ELSEVIER

Contents lists available at ScienceDirect

Ocean Modelling

journal homepage: www.elsevier.com/locate/ocemod



Subgrid corrections in finite-element modeling of storm-driven coastal flooding



Johnathan L. Woodruff ^{a,*}, J.C. Dietrich ^a, D. Wirasaet ^b, A.B. Kennedy ^b, D. Bolster ^b, Z. Silver ^b, S.D. Medlin ^a, R.L. Kolar ^c

- ^a Department of Civil, Construction, and Environmental Engineering, North Carolina State University, 2501 Stinson Drive, Raleigh, NC, 27607, United States of America
- b Department of Civil and Environmental Engineering and Earth Science, University of Notre Dame, South Bend, IN, 46556, United States of America
- c School of Civil Engineering and Environmental Science, University of Oklahoma, Norman, OK, 73019, United States of America

ARTICLE INFO

Keywords: Storm surge Subgrid ADCIRC Wetting and drying Shallow water equations

ABSTRACT

Coastal flooding models are used to predict the timing and magnitude of inundation during storms, both for real-time forecasting and long-term design. However, there is a need for faster flooding predictions that also represent flow pathways and barriers at the scales of critical infrastructure. This need can be addressed via subgrid corrections, which use information at smaller scales to 'correct' the flow variables (water levels, current velocities) averaged over the mesh scale. Recent studies have shown a decrease in run time by 1 to 2 orders of magnitude, with the ability to decrease further if the model time step is also increased.

In this study, subgrid corrections are added to a widely used, finite-element-based, shallow water model to better understand how they can improve the accuracy and efficiency of inundation predictions. The performance of the model, with and without subgrid corrections, is evaluated on scenarios of tidal flooding in a synthetic domain and a small bay in Massachusetts, as well as a scenario with a real atmospheric forcing and storm surge in southwest Louisiana. In these tests we observed that the subgrid corrections can increase model speed by 10 to 50 times, while still representing flow through channels below the mesh scale to inland locations.

1. Introduction

Storm surge, defined as the storm-induced rise in water above the normal astronomical tide, is the principal cause of loss of lives and damages to natural and built infrastructure during coastal storms. Storm surge can cause extensive flooding in regions with relatively flat coastal topography, such as the flooding of southeast Texas during Ike (2008), which pushed floodwaters up to 65 km inland (Hope et al., 2013). As storms become more intense due to climate change (Emanuel, 2020), their associated flooding and impacts will be exacerbated. In the United States, about 7.1 million single-family and 250,000 multifamily residences are at risk of damage from storm surge, and the combined reconstruction costs, assuming complete destruction, of these structures has been estimated at nearly \$1.8 trillion (CoreLogic, 2020). There is a need to predict coastal flooding, both in real-time to aid in emergency management (Cheung et al., 2003), and between storms to aid in long-term planning and mitigation efforts (Helderop and Grubesic, 2019).

Predictive numerical models must represent the evolution of storm surge over a wide range of spatial scales, from its generation in shallow shelfs, bays, and estuaries, to its conveyance into inland regions

via narrow natural and man-made channels, to its interactions with hydraulic controls like dunes, levees, and raised roadways. The ADvanced CIRCulation (ADCIRC) modeling system (Luettich et al., 1992; Westerink et al., 2008) is widely used in coastal flooding predictions due partly to its use of unstructured, finite-element meshes, which can vary resolution from kilometers in the open ocean, to tens of meters in small-scale channels and inland regions. ADCIRC has been wellvalidated for predictions of storm surge along the U.S. Gulf and Atlantic coasts (Dietrich et al., 2011; Hope et al., 2013; Deb and Ferreira, 2016; Cialone et al., 2017), often by using meshes with millions of elements to describe the coastal region of interest. However, this fine resolution (typically as small as 100 to 200 m) can lead to long simulation times. Although ADCIRC is highly scalable in high-performance computing environments (Tanaka et al., 2011; Dietrich et al., 2012), a typical ADCIRC storm surge simulation can require multiple hours of wallclock time on hundreds (or thousands) of CPUs. Because of this, when ADCIRC is used for real-time forecasting (Fleming et al., 2008; Blanton et al., 2012; Dresback et al., 2013), it is limited typically to simulations of the consensus forecast and a few perturbations for each advisory. In

E-mail address: jlwoodr3@ncsu.edu (J.L. Woodruff).

^{*} Corresponding author.

contrast, other less computationally expensive models may consider an ensemble of storm scenarios to account for uncertainties in storm track, forward speed, and intensity. This method of ensemble forecasting is advantageous in that it gives researchers and emergency managers a broader view of potential storm impacts, thereby increasing their preparedness.

At the same time, because ADCIRC and other coastal models are used for predictions on regional (single or multiple state coastlines) domains, it has been computationally expensive for them to represent variability in topography and land cover at the highest available resolution. There has been significant improvement to both the quality and availability of topo/bathy data to describe the coastal zone. Databases, such as NOAA Digital Coast (National Oceanic and Atmospheric Administration, 2020) and the USGS Coastal National Elevation Database (CoNED) (U.S. Geological Survey, 2020a), offer high quality digital elevation models (DEMs) stretching across large swaths of coastline with resolutions typically ranging from 1 to 10 m. These geospatial data resolutions are much smaller than the mesh resolution used by flooding models. For model input, these data can be upscaled to identify the critical flow pathways and barriers that can be represented at the mesh scale (Bilskie et al., 2015), and with the model output, these data can be used to downscale the flooding predictions for decision support (Rucker et al., 2021). However, it has been cost-prohibitive to perform the model computations at the highest resolution of the geospatial data, thus limiting the accuracy of flooding predictions through the smallest channels and over the smallest roughness features.

Thus there is a need for faster flooding simulations that also represent flow pathways and barriers at the highest-resolution of geospatial data sets. This need can be addressed via *subgrid corrections*, which use information at smaller scales to 'correct' the flow variables (water levels, current velocities) averaged over the mesh scale.

Originally implemented to account for irregularities in model domains (Defina, 2000), subgrid corrections have grown increasingly popular due to their abilities to improve accuracy, by better representing flows below the model scale, and/or efficiency, by enabling a similar prediction on a coarsened mesh. The governing shallow water equations are averaged to account for topography and bathymetry smaller than the model scale (Defina, 2000; Casulli, 2009; King, 2001). These averaged equations contain variables that represent the integrated subgrid topography averaged over the computational cell area. Recent studies have shown a decrease in run time by 1 to 2 orders of magnitude when compared to simulations run on fine meshes, with the ability to decrease further if model time step were also increased (Sehili et al., 2014; Wu et al., 2016). Subgrid corrections have been demonstrated for synthetic domains to show proof of concept, and for relatively small, realistic domains like a tidally influenced marsh (Roig, 1994; Bates and Hervouet, 1999; Defina, 2000; King, 2001; Wu et al., 2016; Kennedy et al., 2019). Many of these studies forced their models with either a sinusoidal tidal curve, or with tidal data collected near the domain. Although some studies have forced a single flood wave (Viero, 2019) and relatively minor storm surge events (Sehili et al., 2014), none have considered forcing due to hurricane winds, and thus there are remaining questions about the viability of subgrid corrections for storm-driven flooding.

We explore the use of subgrid corrections for predictions of coastal flooding in realistic domains using ADCIRC. It is hypothesized that, even with a so-called 'Level O' closure that corrects flow behavior only at the wet/dry front, the subgrid corrections will allow ADCIRC to better-represent the smallest flow pathways while using coarser resolution, thus improving both accuracy and efficiency. We describe the implementation of subgrid correction factors into ADCIRC's governing equations. The performance of the model, with and without subgrid corrections, is evaluated on three test domains: an idealized winding channel domain, a small tidally influenced bay in Massachusetts, and a larger domain in southwestern Louisiana to provide a realistic storm surge scenario. It is shown that subgrid corrections can drastically improve storm surge

predictions on coarse meshes. When tested on significantly coarsened meshes, subgrid ADCIRC can match the results of fine counterparts run with traditional methodology, while offering a 10 to 50 times increase in speed.

2. Methods

2.1. ADvanced CIRCulation (ADCIRC)

ADCIRC uses the continuous-Galerkin, finite-element method with linear C^0 triangular elements to numerically solve the 2D Shallow Water Equations (SWE). This set of equations consists of the depth-averaged continuity and momentum equations, which are solved for water surface elevations ζ and depth-averaged velocities U and V for coastal circulation (Luettich and Westerink, 2004). ADCIRC solves the Generalized Wave Continuity Equation (GWCE), a reformulation of the primitive continuity equation into a generalized second-order wave equation, to avoid spurious oscillations associated with the primitive form of the equation (Kinnmark, 1986). This study uses the so-called 'conservative' form of the momentum equations, in which the dependent variables are the fluxes UH and VH (where H is the total water depth), to ease the implementation.

The subgrid corrections will have their greatest effect in partially wet regions, and thus their implementation will require a revision to ADCIRC's wetting and drying algorithm. Traditional ADCIRC uses a complicated but robust system of logic to determine whether mesh vertices are wet or dry (Luettich and Westerink, 1995). It analyzes not only the values of total water depth but also water surface gradients and current velocities to update a wet/dry status of finite-element vertices during the simulation. These checks occur in the middle of each timemarching step, i.e. after the GWCE is solved for updated water surface elevations but before the momentum equations are solved for updated current velocities. A vertex becomes wet if a sufficient water surface gradient is large enough to allow a wetting velocity to its location, and it remains wet if its total water depth is sufficiently large. An element is considered wet only if its three vertices are wet; otherwise it is dry. Thus there cannot be any partially wet vertices or elements, in contrast to other algorithms (see Medeiros and Hagen (2013) for a review of various wetting/drying algorithms). This can lead to inaccuracies in the wet/dry front, especially if it is not resolved sufficiently at the mesh scale. However, Dick et al. (2013) showed in 1D that ADCIRC's wetting and drying algorithm is amenable to a partially wet scheme.

ADCIRC converts wind velocity to wind stress using the drag formulation from Garratt (1977). Wind stress is then applied to vertices in the momentum solver when solving for flow velocity. In this work, this formulation was revised to reduce the wind stress magnitudes in regions with shallow water depths, to mitigate the possibly unstable situation when high winds are blowing over a thin film of water. The wind stress is multiplied by a wind limiter (C_{τ}) in the form of a hyperbolic tangent function (Eq. (1)):

$$C_{\tau} = \tanh\left(\frac{\rho g H}{C_{ws} |\tau_s|}\right),\tag{1}$$

in which τ_s is the unaltered wind stress, ρ is the density of seawater, g is the acceleration due to gravity, H is the total water depth (which can be grid-averaged as defined below), and C_{ws} is a dimensionless constant ($C_{ws} = 2.5e6$ in this study). This limiter asymptotes to unity for low wind speeds and large water depths, but decreases to zero as water level decreases and wind speed increases.

2.2. Averaged variables

We follow the methodology from Kennedy et al. (2019), which formalizes various aspects of earlier subgrid corrections in the context of SWE with unresolved bed profile at the model scale (Defina, 2000; Casulli, 2009; Volp et al., 2013). Flow variables, including the water

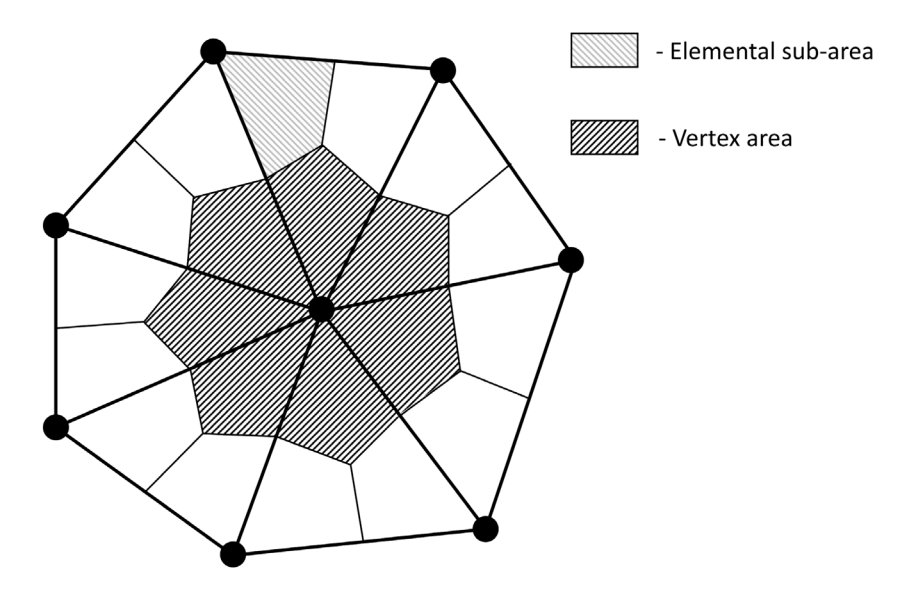


Fig. 1. Schematic of: elemental sub-areas, which are created by dividing each element into three equal pieces; and vertex areas, which are created by combining the elemental sub-areas surrounding each vertex.

surface elevation ζ above mean sea level, the total water depth $H=\zeta+h$ (in which h is the bathymetric depth), and the depth-averaged horizontal velocity components U and V, are averaged to the mesh-scale. It is noted that previous studies have used related but distinct approaches; the flow variable is first integrated over the subgrid cells in the area of interest, and then it is either area-averaged (Defina, 2000) or left as a volume quantity (Casulli, 2009). In this study, we perform an area-averaging.

Kennedy et al. (2019) describe a 'Level 0' closure, in which the mesh-scale areas are allowed to be partially wet. This requires the *a priori* computation of mesh-scale wet areas A_W , which are related to the mesh-scale total areas A_G via the wet-area fraction ϕ :

$$\phi = \frac{A_W}{A_G}. (2)$$

Wet area fractions are pre-computed from a given high resolution topographical dataset typically available as a Digital Elevation Map (DEM). For a possible water surface elevation ζ , wet DEM cells are identified as being within the averaging area and having a positive total water depth. The number of wet cells divided by the total number of cells within the area is taken to be a wet area fraction ϕ . This process is repeated for the full range of possible water surface elevations, thus providing a look-up table to connect wet area fractions ϕ to water surface elevations ζ at every element and vice versa. With the wet area fraction ϕ , we can convert between wet-averaged and grid-averaged quantities. For any flow variable Q, the conversion is:

$$\langle Q \rangle_G = \phi \langle Q \rangle_W, \tag{3}$$

in which the angle brackets $\langle \cdot \rangle$ indicate an averaging to the wet (W) or total (G) area:

$$\langle Q \rangle_G = \frac{1}{A_G} \int_{A_W} Q \, dA \quad \text{and} \quad \langle Q \rangle_W = \frac{1}{A_W} \int_{A_W} Q \, dA.$$
 (4)

There is a challenge to represent the averaged flow variables for an unstructured triangular mesh within a continuous-Galerkin, finite-element framework, due to its vertex-based placement of unknowns (ζ, U, V) . This challenge is overcome via the use of representative areas for both elements and vertices (Fig. 1). Elements are sub-divided into three sub-areas, with each sub-area corresponding to the area nearest a vertex. The elemental sub-areas surrounding a vertex are then combined to form a vertex area.

Averaged total water depth $\langle H \rangle$, averaged Manning's $\langle n \rangle$, and wet area fraction ϕ are pre-computed from a high-resolution DEM and land

cover data for a range of possible water surface elevations (with an increment of 0.05 m in this study). The values are stored in lookup tables, and then referenced at every time step during the simulation.

2.3. Averaged governing equations

In this work, we consider the governing equations arising from applying the formal averaging technique (Whitacker, 1999) to the standard 2D SWE written in the conservative form (see detailed derivation in Appendix). These equations involve averaged flow variables, namely the surface water level $\langle \zeta \rangle_W$, grid-averaged x- and y-directed fluxes $\langle UH \rangle_G$ and $\langle VH \rangle_G$; more precisely, they consist of the averaged horizontal x- and y-momentum equations in the conservative form:

$$\begin{split} &\frac{\partial \langle UH \rangle_{G}}{\partial t} + g \langle H \rangle_{G} \frac{\partial \langle \zeta \rangle_{W}}{\partial x} = -\frac{\partial \langle U \rangle \langle UH \rangle_{G}}{\partial x} - \frac{\partial \langle V \rangle \langle UH \rangle_{G}}{\partial y} + \\ &f \langle VH \rangle_{G} - g \langle H \rangle_{G} \frac{\partial P_{A}}{\partial x} + \phi \left\langle \frac{\tau_{sx}}{\rho_{0}} \right\rangle_{W} - \frac{C_{f} |\langle U \rangle| \langle UH \rangle_{G}}{\langle H \rangle_{W}} \\ &+ \frac{\partial}{\partial x} \left(\widetilde{E}_{h} \frac{\partial \langle UH \rangle_{G}}{\partial x} \right) + \frac{\partial}{\partial y} \left(\widetilde{E}_{h} \frac{\partial \langle UH \rangle_{G}}{\partial y} \right), \end{split} \tag{5}$$

$$\begin{split} &\frac{\partial \langle VH \rangle_{G}}{\partial t} + g \langle H \rangle_{G} \frac{\partial \langle \zeta \rangle_{W}}{\partial y} = -\frac{\partial \langle U \rangle \langle VH \rangle_{G}}{\partial x} - \frac{\partial \langle V \rangle \langle VH \rangle_{G}}{\partial y} - \\ &f \langle UH \rangle_{G} - g \langle H \rangle_{G} \frac{\partial P_{A}}{\partial y} + \phi \left\langle \frac{\tau_{sy}}{\rho_{0}} \right\rangle_{W} - \frac{C_{f} |\langle U \rangle| \langle VH \rangle_{G}}{\langle H \rangle_{W}} \\ &+ \frac{\partial}{\partial x} \left(\widetilde{E}_{h} \frac{\partial \langle VH \rangle_{G}}{\partial x} \right) + \frac{\partial}{\partial y} \left(\widetilde{E}_{h} \frac{\partial \langle VH \rangle_{G}}{\partial y} \right), \end{split} \tag{6}$$

and the averaged continuity equation recast into the GWCE form:

$$\phi \frac{\partial^{2} \langle \zeta \rangle_{W}}{\partial t^{2}} + \frac{\partial \phi}{\partial t} \frac{\partial \langle \zeta \rangle_{W}}{\partial t} + \tau_{0} \phi \frac{\partial \langle \zeta \rangle_{W}}{\partial t} - \frac{\partial}{\partial x} \left(g \langle H \rangle_{G} \frac{\partial \langle \zeta \rangle_{W}}{\partial x} \right) - \frac{\partial}{\partial y} \left(g \langle H \rangle_{G} \frac{\partial \langle \zeta \rangle_{W}}{\partial y} \right) + \frac{\partial \langle \tilde{J}_{x} \rangle_{G}}{\partial x} + \frac{\partial \langle \tilde{J}_{y} \rangle_{G}}{\partial y} - \langle U H \rangle_{G} \frac{\partial \tau_{0}}{\partial x} - \langle V H \rangle_{G} \frac{\partial \tau_{0}}{\partial y} = 0,$$
 (7)

where:

$$\langle \tilde{J}_x \rangle_G = \text{RHS of (5)} + \tau_0 \langle UH \rangle_G \quad \text{and} \quad \langle \tilde{J}_y \rangle_G = \text{RHS of (6)} + \tau_0 \langle VH \rangle_G,$$

in which f is the Coriolis parameter, g is the acceleration due to gravity, τ_{sx} and τ_{sy} are surface stresses, ρ_0 is a reference density, C_f is the bottom friction coefficient, E_h is the lateral stress coefficient, and τ_0 is a positive (spatially varying) parameter weighting the primitive

continuity equation. In the above equations, the grid-averaged total water depth $\langle H \rangle_G$ (and $\langle H \rangle_W = \langle H \rangle_G/\phi$) is assumed known for a given value of $\langle \zeta \rangle_W$. For the depth-averaged velocity, instead of using the formal definition of the averaged quantity (as in Eq. (4)), the averaged $\langle U \rangle = (\langle U \rangle, \langle V \rangle)$ corresponds to the so-called volume-averaged velocity, more specifically $\langle U \rangle = \langle U H \rangle_G/\langle H \rangle_G$. This definition reduces to a point-wise definition of velocity in the limit of the averaging area approaching zero $A_G \to 0$; see Appendix for more detailed discussion.

Note that Eqs. (5)–(7) are structurally similar to the form of the shallow water equations considered in ADCIRC except for the additional parameter ϕ and term $\partial \phi/\partial t$, the latter representing the time rate of change of the wet area fraction. The spatial and temporal discretization of this term is described in A.4. It is noted that these equations are nonlinear, both before and after the averaging; however, we avoid solving this nonlinear system through the time discretization scheme, which converts the equations into a linear algebraic system. The addition of the time derivative term in ϕ was an extra linearization step. As demonstrated later, it is important to note that C_f must be determined carefully, because a straightforward mesh-scale average formula does not necessarily ensure satisfactory results. Indeed, this aspect is the focus of ongoing research (Sehili et al., 2014; Viero, 2019; Volp et al., 2013).

The GWCE is solved implicitly via the use of a global mass matrix, while the momentum equations are solved semi-implicitly. In this study, the ADCIRC solvers were kept the same, but averaged variables were substituted for their non-averaged counterparts. Both element- and vertex-based quantities are used in these solutions. On each time marching step, the GWCE (Eq. (7)) uses elementally-averaged quantities to find a vertex-averaged water surface elevation $\langle \zeta \rangle_W$. This quantity is then used to look up the corresponding vertex-averaged total water depth $\langle H \rangle_G$ and wet area fraction ϕ , which are used along with elementally-averaged quantities to solve Eqs. (5) and (6) for the vertex-averaged water velocities. Because we are solving averaged equations, the solutions for $\langle \zeta \rangle_W$, $\langle U \rangle$, and $\langle V \rangle$ are appropriately averaged. Therefore, no further manipulation to the solutions is required.

A primary contribution of this work is the use of a logic-free wet/dry algorithm. The new algorithm determines the wet/dry state by enforcing a minimum wet area fraction of the element:

$$\phi > \phi_{\min}$$
. (8)

This minimum fraction ϕ_{min} is set by the user and can be adjusted depending on the application, e.g. a minimum wet area fraction $\phi_{min}=0.05$ would require that only 5% of an element must be submerged for it to be active and included in calculations. This new algorithm improves the code in several ways: replaces the existing algorithm and its extensive logic statements, gives a more accurate representation of the wet/dry front, smooths the transition between wet and dry elements and vertices, and allows ADCIRC to resolve subgrid hydraulic features.

2.4. Test cases

Three test cases are used to evaluate the effectiveness of ADCIRC with subgrid corrections. The first test case is a plane sloping beach with a small winding channel of width 250 m in the middle of the domain. The domain is described by a synthetic 10-m DEM, which is then used to develop meshes with varying resolution to either fully or inadequately resolve the channel (Fig. 2).

The second test case is a tidal simulation for Buttermilk Bay, Massachusetts. This domain is chosen because it has several well-defined, small-scale channels, which must be represented in numerical models for accurate predictions of flows into back bays (Kennedy et al., 2019). Coarse and fine meshes are generated for this domain, with bathymetry interpolated from a 3-m DEM (Fig. 4). The topo/bathy data are obtained from NOAA Digital Coast (National Oceanic and Atmospheric Administration, 2020).

The third test case is chosen as a realistic scenario for storm surge predictions. Using a 3-m DEM from USGS CoNED (U.S. Geological Survey, 2020a), two ADCIRC meshes are created using OceanMesh2D (Roberts et al., 2019) for Calcasieu Lake and the connected Bayou Contraband in southwestern Louisiana. Its location along the Gulf of Mexico, low-lying topography, and shallow, flat bathymetry make it highly vulnerable to storm surge. There are also numerous well-defined, small-scale channels in this region including Calcasieu Pass, Bayou Contraband, and intra-coastal waterways. With traditional ADCIRC, this domain requires a fine mesh (with resolution down to 50 m) to represent the hydraulic connectivity. There also exist water elevation data both at the coast and far up the bayou, which will serve to validate the results of the subgrid model.

2.5. Error metrics

The accuracy and efficiency of the model will be evaluated in each test case. To evaluate accuracy with and without the sub-grid corrections on coarse meshes, we select three error metrics that are focused on the conveyance of tides and flood waters through channels below the model scale. First, for tides, we compute the duration (in hours) that channel locations are wet during one tidal cycle. We compare to predictions from a fine-mesh simulation, and thus an optimal result is a perfect match between durations on the coarse and fine meshes. Second, for flood waters, we consider the predicted peak water levels at channel locations. We compare to either the results from a fine-mesh simulation or to gauge observations, and an optimal result is a zero difference between peaks. Third, for both tides and flood waters, we consider the predicted maximum water levels along channel thalweg transects, i.e. the line connecting the deepest parts of the channel, again to examine the conveyance. We compare to results from a fine-mesh simulation by computing a root-mean-square error ($E_{\rm RMS}$) using all points along the transect, and thus an optimal result is an $E_{\rm RMS}=0$.

$$E_{\text{RMS}} = \sqrt{\frac{\sum_{i=1}^{N} (x_i - \hat{x}_i)^2}{N}},$$
 (9)

in which N is the number of points along the transect, and x and \hat{x} are the predicted maximum water levels from simulations on coarse and fine meshes, respectively. With these three error metrics, we assess the accuracy of predictions of flow through small-scale channels to inland level times.

Model efficiency was measured by wall-clock timings. Simulations were run on Intel Xeon E5-2650 v2 processors, which have 8 dual-thread cores per processor, 20 MB of cache, and a frequency of 2.60 GHz. The processors are connected via an IB6131 Infiniband switch in the High-Performance Computing Services at North Carolina State University, but all simulations were run in serial to remove the inter-core communication times from the comparisons. For the timing comparisons, each simulation was run in triplicate, and the average wall-clock time was reported.

3. Results

3.1. Winding channel

The first test has a 12-km by 12-km plane sloping beach with a 250-m winding channel (Fig. 2). A synthetic DEM was created with a resolution of 10 m and with minimum and maximum elevations of -5 m and 2 m, respectively. The channel thalweg is always 1 m below the surrounding ground surface, and it was included to test the ability of the subgrid ADCIRC to represent flows below the mesh scale.

Two meshes are developed (Fig. 2): a coarse mesh with average element side length of 1000 m, and a fine mesh designed to fully resolve the winding channel with a minimum resolution of 50 m and maximum of 500 m. The coarse mesh has 192 vertices and 334 elements, while the fine mesh has 12,475 vertices and 24,852 elements. Thus, the

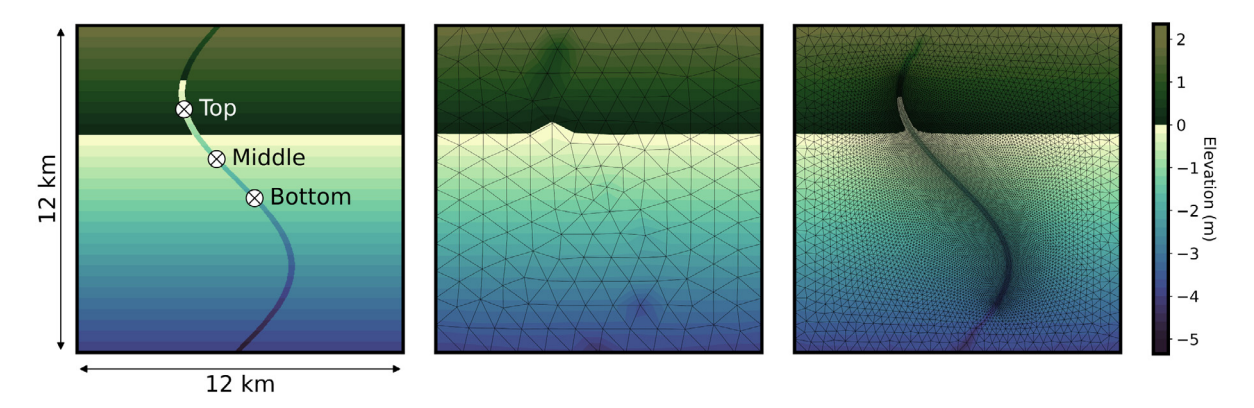


Fig. 2. For the winding channel test case, (left) DEM and locations where water surface elevations were recorded, (center) coarse-resolution mesh, and (right) fine-resolution mesh. Contours indicate the ground surface elevations (m relative to mean sea level).

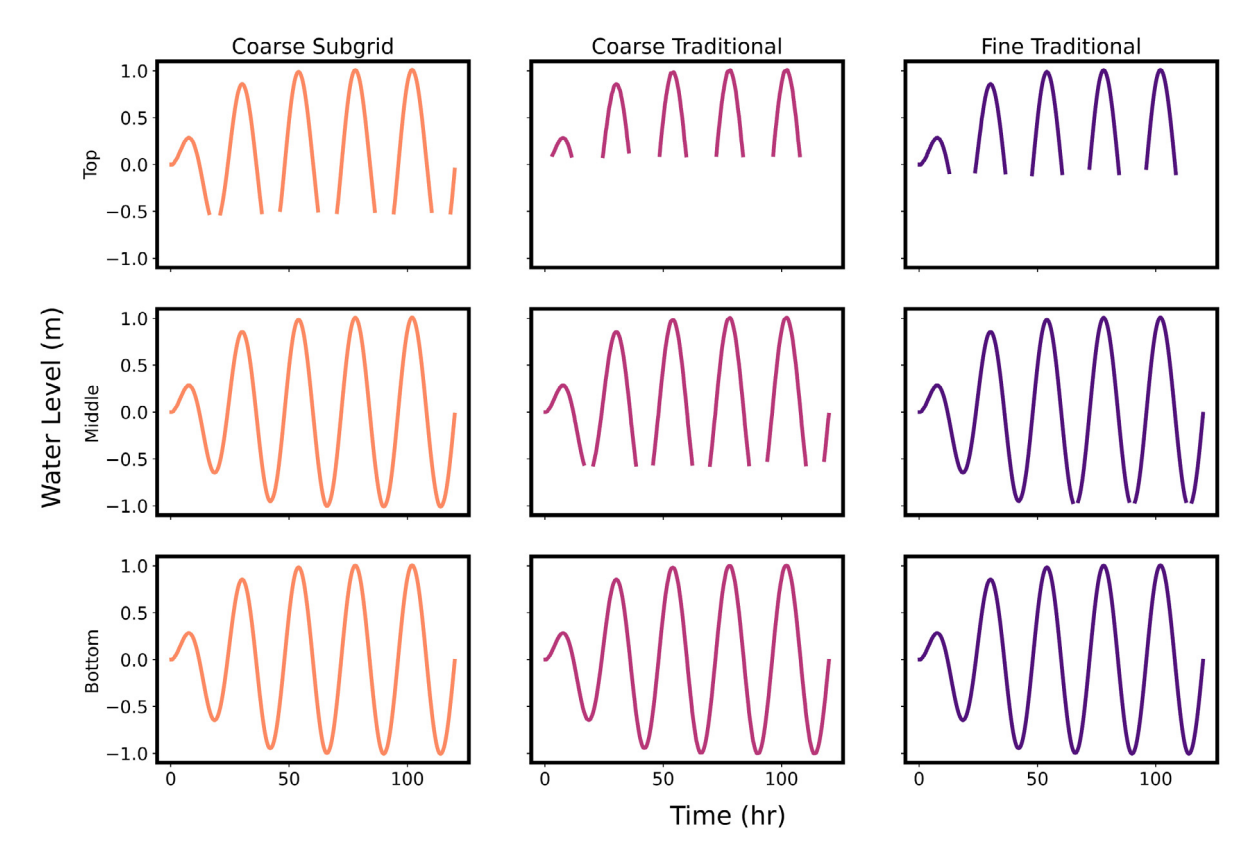


Fig. 3. For the winding channel test case, time series of water levels (m relative to mean sea level). Order of plots from top to bottom matches the station locations in Fig. 2.

number of degrees of freedom of the coarse mesh is approximately 65 times less than that of the fine mesh. The bathymetry for both meshes is set using Inverse Distance Weighted (IDW) interpolation from the DEM (Burrough and McDonnell, 1998).

We consider simulations of three run configurations: (1) fine traditional, (2) coarse traditional, and (3) coarse subgrid. Each simulation is forced by a 5-day diurnal tidal signal with amplitude of 1 m, with a 2-day ramp to prevent abrupt introduction of elevation forcing. Bottom friction is computed with a constant Manning's coefficient of n=0.012, and horizontal eddy viscosity is set to a constant value of $\tilde{E}_h=20~\text{m}^2/\text{s}$. For traditional simulations, the wet and dry states are controlled by requiring a minimum wetting velocity of 0.1 m/s and a minimum water depth of 0.1 m, respectively. For the subgrid simulation, the minimum wet area fraction $\phi_{\text{min}}=0.05$.

Predicted water levels were recorded at stations along the channel thalweg and near the Top, Middle, and Bottom of the tidal range (Fig. 2). The hydrographs show the ability of the subgrid corrections

to represent the tidal behavior in this small channel (Fig. 3). At the station near the top of the tidal range, the ground surface is -0.5 m relative to mean sea level. Because the domain is small enough to prevent a significant lag between the boundary forcing and the water levels within the domain, this station should be wetted for the 16 hr surrounding each peak tide. However, considering the fourth tidal peak (when the model forcing is at full strength), this wet duration is varied among the simulations (Table 1). The fine traditional simulation can represent about 12.5 hr, wetting when the water level rises to -0.04 m and drying when the water level falls to -0.10 m. The inability of the fine traditional simulation to represent the full 16 hr of the tidal peak at this location is likely due to: inaccuracies introduced when upscaling the synthetic ground surface to its 50-m resolution; and the binary nature of traditional ADCIRC's wet/dry algorithm, which can limit the predictions of the wetting front. The coarse traditional simulation can represent less of the high tide, or about 11.25 hr, wetting when the water level rises to 0.1 m and drying when the water level falls to

Table 1
For the winding channel test case, accuracy results for: wet duration (hr) during the fourth tidal period for each station, peak-to-peak difference (m) between coarse simulation and fine simulation, and E_{RMS} (m) of maximum water level along main channel thalweg between coarse simulations and fine simulations.

Simulation	Wet duration (hr)			Peak-to-Peak difference (m)			E _{RMS} (m)
	Тор	Middle	Bottom	Тор	Middle	Bottom	
Coarse subgrid	16	24	24	8.0e-4	3.0e-4	8.9e-4	7.4e-5
Coarse traditional	11.25	16.5	24	7.0e-4	2.6e-3	3.0e-3	1.2e-3
Fine traditional	12.5	21.5	24	_	_	-	-
Theoretical	16	24	24	_	_	-	-

Table 2For all test cases, wall-clock times (sec) for ADCIRC simulations on a serial processor, and ratios of wall-clock times. The average time of three simulations was reported.

	Winding channel	Buttermilk Bay	Calcasieu lake
Wall-Clock times (sec)			
Coarse subgrid	107	508	5248
Coarse traditional	62	277	3728
Fine traditional	5787	4176	167,514
Ratios of Wall-Clock times			
Coarse subgrid/Coarse traditional	1.73	1.83	1.41
Fine traditional/Coarse subgrid	54.1	8.22	31.9

0.096 m. In contrast, the coarse subgrid simulation is able to represent the full 16 hr of high tide, wetting when the water level rises to -0.51 m and drying when the water level falls to -0.49 m.

The middle station is located where the ground surface is -1.45 m relative to mean sea level. This station should stay wet throughout the duration of the tidal cycle. However, both the fine traditional and the coarse traditional simulations become dry at the middle station. The fine traditional simulation represents 21.5 hr of the signal, becoming wet with the flood tide at a water surface elevation of -0.95 m and drying with the receding tide when the water level falls past the same elevation of -0.95 m. The coarse traditional simulation represents only 16.5 hr of the tidal cycle. The middle station becomes wet at a water level of -0.57 m and dries when the water level falls back to -0.56 m. The coarse subgrid simulation is able to represent the full tidal cycle at the middle station and does not dry at any time.

The bottom station is located where the ground surface elevation is -2.165 m relative to mean sea level. This station lies well beneath the lowest part of the tidal signal, and should never dry. All three simulations were able to represent the full tidal range at the bottom station.

For the peak-to-peak differences and thalweg $E_{\rm RMS}$ relative to the fine mesh (Table 1), the values were about one order of magnitude smaller with the subgrid corrections, e.g. the channel thalweg $E_{\rm RMS}$ = 7.4e–5 for the coarse subgrid, but $E_{\rm RMS}$ = 1.2e–3 for the coarse traditional. However all of these peak-to-peak differences and thalweg $E_{\rm RMS}$ were very small for both simulations.

The subgrid corrections add computational time when compared to traditional ADCIRC simulations on the same mesh (Table 2). The increase in run time is attributed to reading the lookup tables, referencing to the tables at every time step of the simulation, and interpolating between table increments. For the coarse winding channel test case, subgrid ADCIRC ran 73% more slowly than its traditional counterpart. The efficiency of the subgrid implementation can likely be increased with better coding practices and smaller lookup table file sizes. However, the subgrid ADCIRC allowed flooding in the winding channel for more of the tidal cycle than a traditional simulation on a mesh with 65 times finer resolution, and it produced results 54 times faster. Thus the decrease in efficiency at the same mesh resolution is more than overcome by the increase in accuracy at coarser mesh resolutions for the subgrid corrections.

3.2. Buttermilk Bay

Buttermilk Bay is a small bay near the community of Bourne, Massachusetts (Fig. 4). It is connected via the Cape Cod Canal to Cape

Cod and Buzzards Bay to the north and south, respectively. A channel with a width of 250 m connects into a main bay with surface area of 1.54 km². From the main bay, a smaller channel with a width of 50 m connects into a smaller inner bay with a surface area of 0.42 km². Thus it is a good test to represent the propagation of tidal flows through channels below the model scale.

A high-resolution, 3-m DEM from NOAA Digital Coast is used to represent the bathymetry and topography, and two unstructured meshes are developed from this DEM (Fig. 4). In the coarse mesh, the elements are 'paved' over the region, with no attempt to align their locations or sizes with the ground contours. The average element side length for the coarse mesh is about 100 m. In the fine mesh, vertices are aligned with the 0 m elevation contour to ensure that channels and coastlines are properly defined. The fine mesh has a minimum element side length of 10 m and a maximum of 50 m. The coarse mesh has 830 vertices and 1569 elements, while the fine mesh has 4795 vertices and 9412 elements.

The model parameters for the Buttermilk Bay simulations are similar to the winding channel test case. A diurnal tidal signal of 1 m amplitude with a 2-day ramping period is forced at the ocean boundary. Constant Manning's n=0.022 is applied over the entire domain. Horizontal eddy viscosity is set to $\tilde{E}_h=2.0~\text{m}^2/\text{s}$ for the fine simulation and $\tilde{E}_h=50~\text{m}^2/\text{s}$ for the coarse simulation. For the traditional ADCIRC, the wet/dry parameters of minimum water depth and minimum velocity are set to 0.1 m and 0.1 m/s, respectively. For subgrid ADCIRC, the minimum wet area fraction $\phi_{\text{min}}=0.05$.

Water level results are evaluated at three stations in Buttermilk Bay (Fig. 4). These stations are selected to evaluate the ability of subgrid ADCIRC to predict flow through regions with hydraulic features that are smaller than the resolution of the coarsened mesh. The Main station, located in the fully wet area of the domain, serves as a baseline to show all models were forced properly. The Arm station is in a small, tidally influenced stream that is between 5 m and 10 m wide. The Back station lies in Little Buttermilk Bay and is separated from the main bay by a 50-m wide channel.

At the Main station, the water level time series is matched in all three simulations in both amplitude and phase (Fig. 5 and Table 3). However, only the coarse subgrid and fine traditional simulations can capture hydraulic connectivity to the stations located in or near small channels.

At the Arm station, again considering the fourth tidal peak (when forcing is at its full strength), there is variability in the predictions. The coarse traditional simulation was unable to represent any water at the Arm station throughout the duration of the tidal signal. The fine

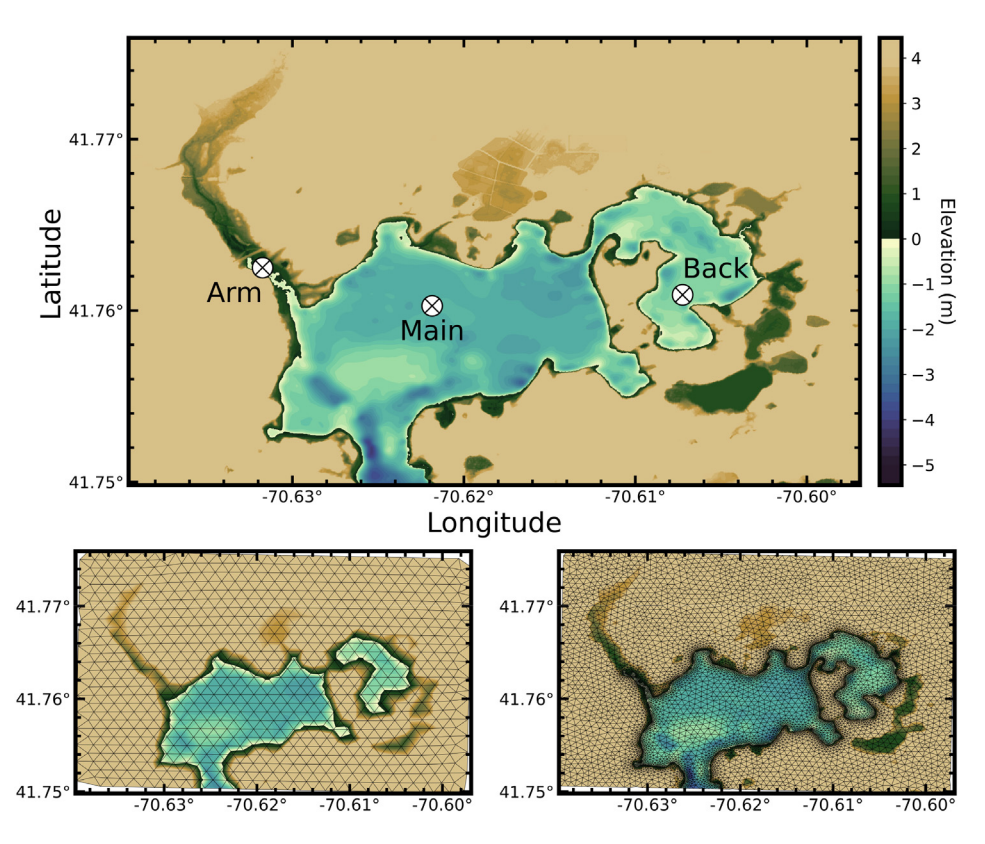


Fig. 4. For the Buttermilk Bay test case, (top) DEM in WGS84 coordinates and locations where water surface elevations were recorded, (bottom left) coarse-resolution mesh, and (bottom right) fine-resolution mesh. Contours indicate the ground surface elevations (m relative to NAVD88).

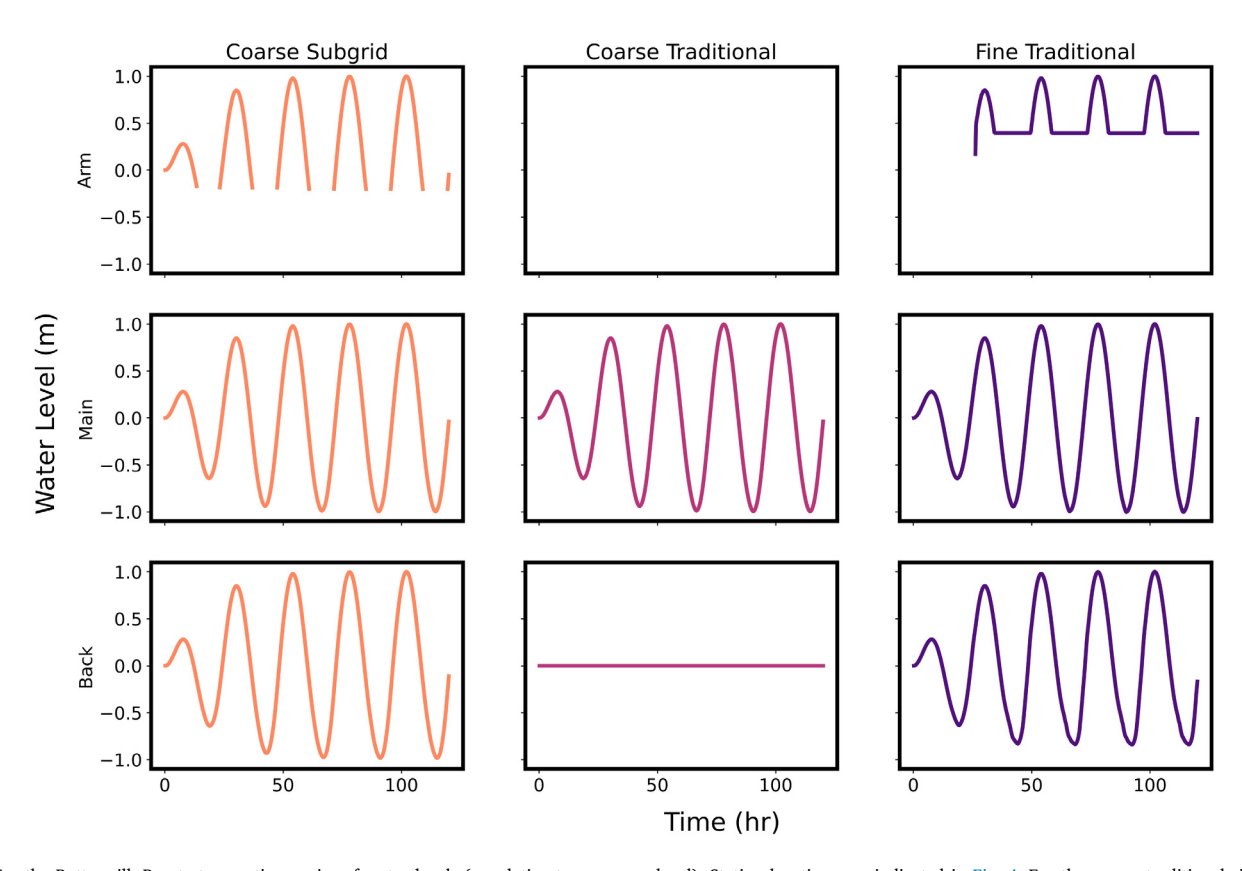


Fig. 5. For the Buttermilk Bay test case, time series of water levels (m relative to mean sea level). Station locations are indicated in Fig. 4. For the coarse traditional simulation, the Arm station is always dry, while the Back station is wet but disconnected from the tidal forcing.

Table 3
For the Buttermilk Bay test case, accuracy results for: wet duration (hr) during the fourth tidal signal for each station, peak-to-peak difference (m) between coarse simulation and fine simulation, and E_{RMS} (m) of maximum water level along the arm and back bay thalweg between coarse simulations and fine simulations.

Simulation	Wet duration (hr)			Peak-to-Pe	Peak-to-Peak difference (m)			$E_{\rm RMS}$ (m)	
	Arm	Main	Back	Arm	Main	Back	Arm	Back	
Coarse subgrid	13.75	24	24	1.4e-5	5.2e-4	1.6e-3	6.5e-4	8.9e-4	
Coarse traditional	0	24	24	_	5.3e-4	1.0e0	6.8e-4	5.5e-1	
Fine traditional	24	24	24	_	_	_	_	-	

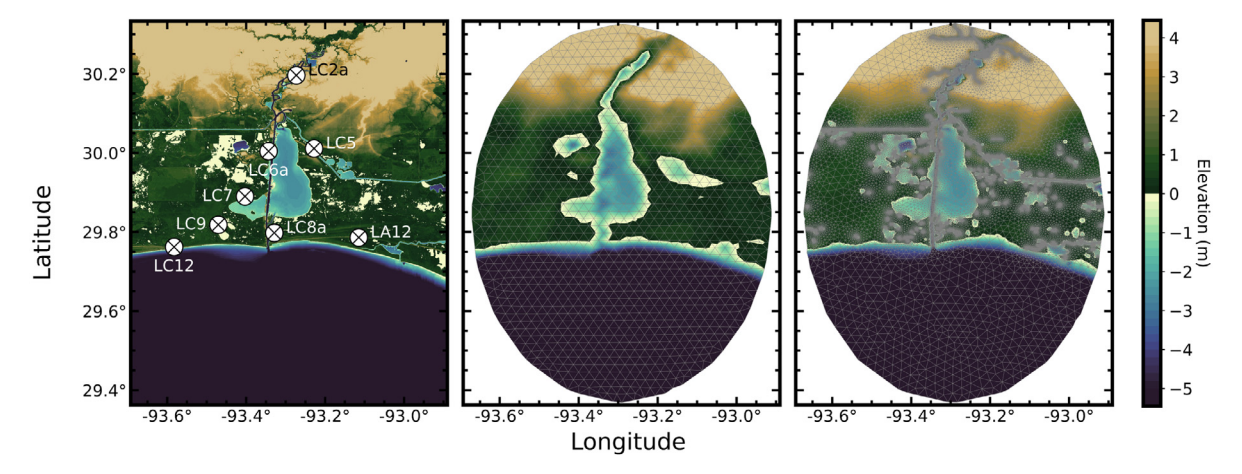


Fig. 6. For the Calcasieu Lake test case, (left) 3-m DEM from USGS CoNED with gauge numbers and locations indicated by the crossed circles, (center) coarse-resolution mesh; and (right) fine-resolution mesh. Contours indicate the ground surface elevations (m relative to NAVD88).

traditional simulation is able to represent connectivity to the Arm for about 9 hr during the crest of the fourth tidal peak. It loses hydraulic connectivity from the Arm to the Main Bay at hour 82.5 and maintains a steady water surface elevation of 0.39 m for 15 hr until the return of the flood tide at hour 97. The surface elevation is maintained because, after connectivity is lost, water becomes trapped and cannot drain to the Main Bay, therefore this station remains wet throughout the simulation (Table 3). The coarse subgrid simulation maintains connectivity for 13.75 hr during the fourth tidal peak. Its Arm was fully dried at hour 85 and water surface elevation of -0.2 m for 10.5 hr until hour 95.5, when it floods again with the incoming high tide. Thus, at the Arm, the coarse subgrid simulation shows improved connectivity when compared to the coarse traditional and fine traditional simulations (Table 3).

At the Back station, the coarse traditional simulation indicates that there is water but no tidal flow, and thus the peak-to-peak difference is 1 m and the thalweg $E_{\rm RMS}=5.5\rm e{-}1$ m. The coarse subgrid and fine traditional simulations are able to represent flow through the small channel that connects from the main bay. For the coarse subgrid simulation, the errors are reduced by three orders of magnitude; the peak-to-peak difference is $1.6\rm e{-}3$ m and the $E_{\rm RMS}=8.9\rm e{-}4$ m.

The subgrid corrections increase the computational time when compared to traditional ADCIRC simulations on the same mesh (Table 2). For the coarse mesh, subgrid ADCIRC ran 83% more slowly than its traditional counterpart. However, it produced results that showed greater connectivity through small channels than a traditional simulation run on a mesh with 6 times the resolution, and its results were produced more than 8 times faster. The coarse mesh can likely be coarsened further, but was constrained by the width of the lateral boundary where the tidal forcing was applied. If this constraint was not present, further efficiency gains between the coarse subgrid and fine traditional simulations could be achieved.

3.3. Calcasieu Lake

Calcasieu Lake is a large, 242 km², tidally influenced water body in southwest Louisiana. The south end of the lake is connected to the Gulf of Mexico by Calcasieu Pass, which is an 8.5-km-long, 300-m-wide

shipping channel that is maintained for commerce and recreation. The north end of the lake is connected to the community of Lake Charles by Bayou Contraband, a natural riverine system that is about 300 m wide and extends 20 km northward to Lake Charles. The east and west sides of the lake are connected to neighboring water bodies by maintained 200-m-wide intracoastal waterways.

The storm used in this test case was Rita (2005), which made landfall near the Texas/Louisiana border as a Category 3 hurricane on the Saffir–Simpson scale (Knabb et al., 2005). Lake Calcasieu and its neighboring communities were highly impacted by this storm due to their position in the northeast quadrant of the wind field and their low lying, flat topography. Maximum water levels reached 4.7 m along the coast with flood waters extending as far as 80 km inland (Dietrich et al., 2010; Berenbrock et al., 2008).

Similar to Buttermilk Bay, a coarse-resolution mesh is paved over the domain with no consideration of bathymetric details. The average element side length for the coarse mesh is 2000 m. A fine mesh is created with a minimum element side length of 50 m and a maximum of 2000 m. Vertices in the fine mesh are aligned along the 0-m elevation contour to ensure that channels and coastlines were properly defined. The fine mesh has a similar resolution and development as in larger studies of storm surge in the same region (Hope et al., 2013). The coarse resolution mesh has 1236 vertices and 2370 elements, while the fine mesh has 40,816 vertices and 81,321 elements (Fig. 6).

The model parameters for the Calcasieu Lake meshes are interpolated from an ocean-scale, fine mesh available for this region. These model parameters include wind reduction factors derived from land-use/land-cover data, horizontal eddy viscosities in classes of $\tilde{E}_h=2,20,50~\text{m}^2/\text{s}$, and values for the primitive weighting in the GWCE in classes of $\tau_0=0.005,0.02,0.03$. Manning's n coefficients for the meshes were derived from a 2006 Coastal Change Analysis Program (C-CAP) regional land cover dataset downloaded from the NOAA Digital Coast (National Oceanic and Atmospheric Administration, 2021). Values were interpolated onto the mesh vertices using a harmonic average of the Manning's n values contained in the surrounding vertexelements. For the subgrid simulation, wet averaged Manning's n values

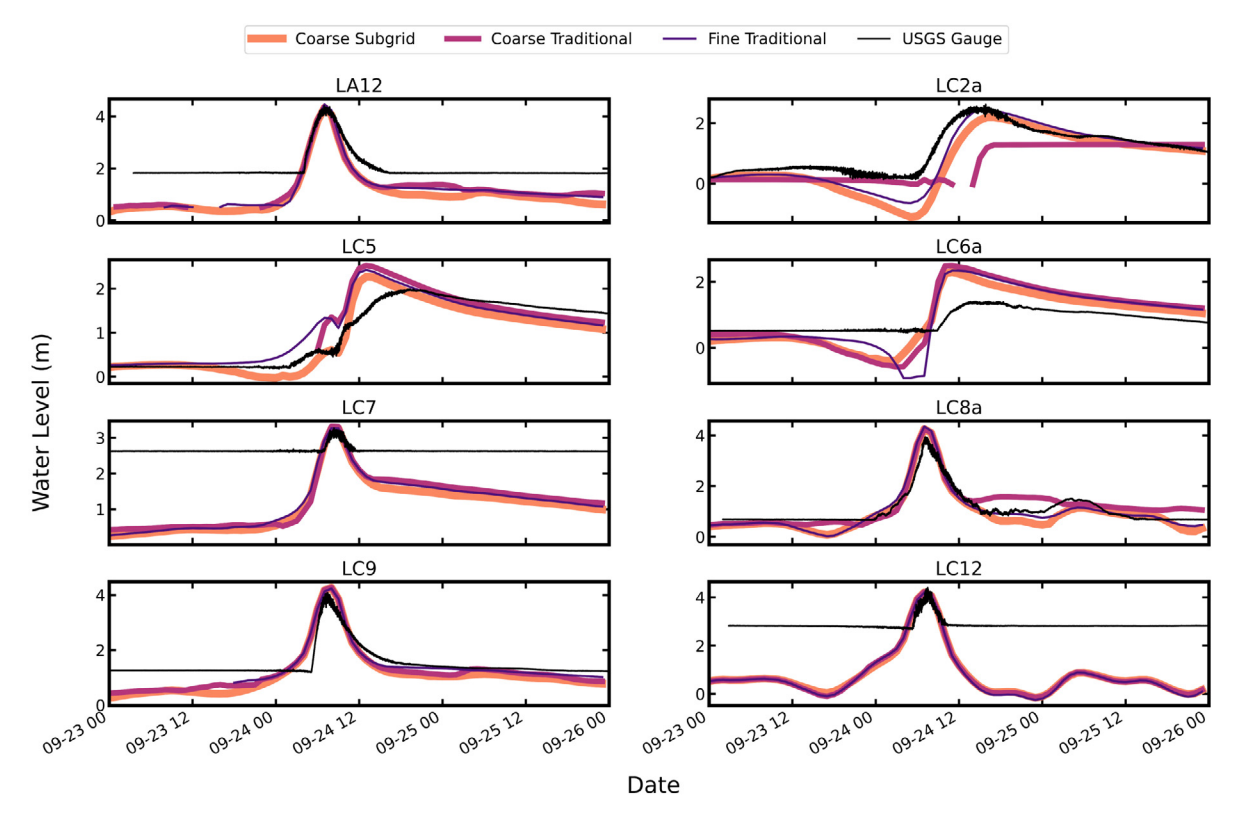


Fig. 7. For the Calcasieu Lake test case, time series of water levels (m relative to mean sea level) at USGS gauges with locations shown in Fig. 6.

were computed prior to the simulation and looked up based on water surface elevations (Eq. (10)):

$$\frac{g\langle n\rangle_W^2 |\langle \mathbf{U}\rangle\langle UH\rangle_G}{\langle H\rangle_W^{4/3}},\tag{10}$$

in which $\langle n \rangle_W$ is the wet averaged Manning's n. This was done to prevent overestimation of bottom friction in the subgrid model. Traditional simulations use a minimum water depth and a minimum velocity for wetting of 0.1 m and 0.1 m/s, respectively, while the subgrid model uses a threshold $\phi_{\rm min}=0.05$.

The model is forced along its ocean boundary with water surface data taken from an ocean-scale ADCIRC simulation of Rita and winds produced by a Generalized Asymmetric Holland Model (GAHM) of the same storm (Gao, 2018). At every vertex, GAHM computes wind velocities and surface atmospheric pressures; the wind velocities are then scaled based on surface roughness and canopy cover present in the area. Parametric models such as GAHM can generate a reasonable representation of a hurricane wind field provided that proper wind parameters are used (Lin and Chavas, 2012), and in this case, GAHM will provide a realistic forcing with which to evaluate the subgrid ADCIRC. The simulation is run for a total of 23 days, with water surface elevations recorded from locations in the mesh corresponding to USGS gauges deployed prior to the storm (U.S. Geological Survey, 2020b), as well as locations spaced every 2000 m along the main channel thalweg from the Gulf of Mexico to Lake Charles, LA.

Predicted water levels are compared with hydrographs at the USGS gauges (Fig. 7). Water levels at gauge stations LA12, LC7, LC8a, LC9, and LC12 were similar between simulations with differences less than 15 cm (Table 4). These gauges are located near the open coast, so when the 5 m storm surge propagated in, connectivity and subgrid corrections played less of a role in altering the overall water level. However, this is not the case for gauges LC2a, LC5, and LC6a, which are located further inland. At these locations, the coarse subgrid outperforms the coarse traditional simulation by more than 20 cm. Again, this is expected because, as the surge propagates further inland, the

Table 4For the Calcasieu lake test case, peak water level differences (m) for all simulations compared to the recorded gauge water levels during Rita (2005).

	Coarse subgrid	Coarse traditional	Fine traditional
LA12	0.065	0.028	0.060
LC2a	0.423	1.328	0.152
LC5	0.281	0.538	0.435
LC6a	0.898	1.095	0.940
LC7	0.006	0.048	0.002
LC8a	0.312	0.327	0.412
LC9	0.180	0.192	0.155
LC12	0.202	0.182	0.206

influence of subgrid features and flow connectivity have greater effects on the flow.

The most notable difference between the coarse subgrid and coarse traditional simulation is at the LC2a gauge located north of Calcasieu Lake (Fig. 7). This gauge is farthest from the open coast and is connected via the narrow Bayou Contraband, and it recorded a maximum water level of 2.55 m during the storm. At this location, the coarse traditional simulation goes dry at 1100 UTC 24 September at a water level of 0 m and then rapidly wets at 1400 UTC 24 September during the peak of the storm surge. The maximum water level of the coarse traditional simulation remains more than 1 m below the maximum surge predicted by the fine traditional simulation at this gauge, and is hydraulically disconnected from Calcasieu Lake.

The fine traditional and coarse subgrid simulations predicted a peak surge of 2.45 m and 2.18 m, respectively. Thus the coarse subgrid results are too low by about 0.27 m at this location when compared to the fine traditional results, likely due to high winds pushing water out of Calcasieu Lake (causing an excessive draw down), and a minimum wet threshold of $\phi_{\min}=0.05$, which may not fully capture the subgrid processes in Bayou Contraband.

To further evaluate the three simulations, maximum water levels were taken along the main channel thalweg from the Gulf of Mexico to

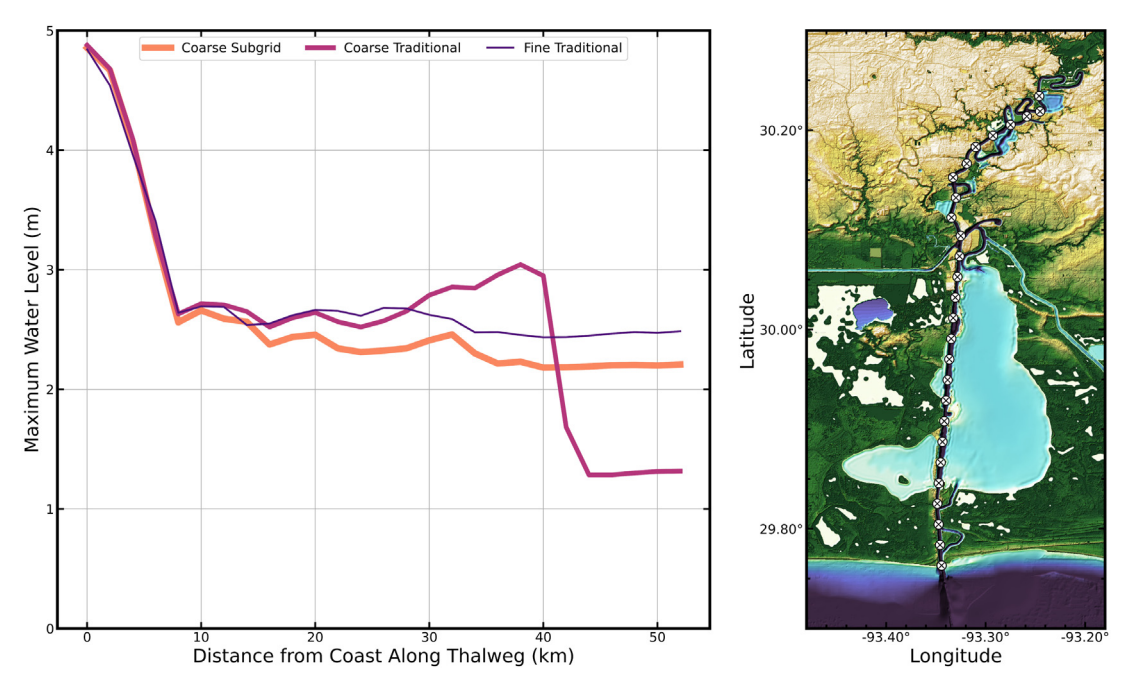


Fig. 8. For the Calcasieu Lake test case, (left) maximum water levels (m relative to mean sea level) along the main channel thalweg, and (right) location of thalweg along the Calcasieu shipping channel and into Bayou Contraband.

Lake Charles, LA (Fig. 8). From the north end of Lake Calcasieu to Lake Charles, the maximum water levels from the coarse subgrid simulation are 0.25 m below that from the fine traditional simulation, while the coarse traditional simulation underpredicts water levels by more than 1 m compared to the fine simulation. For the $E_{\rm RMS}$ along the main channel thalweg, the coarse subgrid $E_{\rm RMS}=0.220$ m, while the coarse traditional $E_{\rm RMS}=0.564$ m. This further demonstrates the superiority of the subgrid simulation at conveying flows through narrow channels.

For these simulations, the subgrid corrections add about 40% to the run-time when compared to the coarse traditional simulation (Table 2). However, the coarse subgrid was about 32 times faster than the fine traditional and was able to connect flow from the Gulf of Mexico, through Lake Calcasieu, and up the Contraband Bayou.

4. Discussion

In these test cases, the subgrid ADCIRC consistently out-performs its traditional counterpart in terms of hydraulic connectivity and maximum water level accuracy, and it allows for efficiency gains by using coarser meshes to represent coastal regions. These advancements have implications for the prediction of storm surge and coastal flooding, both in real-time forecasting and for long-term planning.

The subgrid corrections can be used for predictions with realistic storm forcing in realistic coastal domains. This is an extension of recent subgrid modeling studies, which have used water levels applied at the open boundary from idealized sinusoidal tidal curves or water level data from field measurements (Defina, 2000; Casulli, 2009; Kennedy et al., 2019; Wu et al., 2016). Sehili et al. (2014) used atmospheric forcing from a storm event in the North Sea; however this storm event was not on the scale or power of a tropical cyclone.

In our third test case, subgrid ADCIRC was forced with hurricanestrength winds and storm surge from Rita (2005). The model was able to represent the storm's effects on flow at the coast, more specifically, the flooding of the low-lying topography of southwest Louisiana, and the flow through channels smaller than the model scale. The largest discrepancy between coarse traditional and subgrid simulations was at the LC2a gauge where the model resolution was about seven times larger than the 300-m-wide Bayou Contraband.

Subgrid ADCIRC also allows for a coarsening of the meshes used to describe the coastal region. For the winding channel test case, nearly identical maximum water levels were predicted in the channel by the coarse subgrid and the fine traditional simulations, with improved connectivity in the coarse subgrid simulation (Fig. 3), despite the coarse subgrid simulation having 65 times fewer degrees of freedom and a minimum resolution that was 20 times coarser. The simulation of Buttermilk Bay also showed virtually no difference in maximum water levels between the coarse subgrid and fine traditional simulations, despite the coarse subgrid simulation having almost 6 times fewer degrees of freedom and a minimum resolution that was 10 times coarser. Again, the subgrid showed better hydraulic connectivity, especially in locations in small-scale channels, than the fine traditional. For the Calcasieu Lake test case, the coarse subgrid and fine traditional showed good comparison to gauge observations from Hurricane Rita (2005), despite the coarse subgrid simulation having 33 times fewer degrees of freedom and a minimum resolution that was 40 times coarser. The subgrid simulation was able to represent flows to the inland LC2a gauge, because it allowed flow through the Bayou Contraband below the model scale. These results are similar to those by Kennedy et al. (2019), Sehili et al. (2014), and Wu et al. (2016) who found that the subgrid corrections allowed for a coarsening of meshes by at least 1 order of magnitude.

These advancements have implications for real-time forecasting and long-term engineering and design. When ADCIRC is run traditionally with fine-resolution meshes, each simulation can require thousands of compute cores and hours of wall-clock time (Hope et al., 2013). During a storm event, this requirement can limit its use in a probabilistic forecasting framework, which can account for slight variations in storm track, intensity, and timing (Fleming et al., 2008), and which is used by other forecast models like the Sea, Land, and Overland Surges from Hurricanes (SLOSH) model (National Hurricane Center, 2020). Subgrid ADCIRC may enable probabilistic forecasting. Between storms, agencies like the United States Army Corps of Engineers (USACE) and the Federal Emergency Management Administration (FEMA) use ADCIRC to better prepare coastal cities and communities from future flooding events (U.S. Army Corps of Engineers, 2015; Federal Emergency Management Agency, 2019), typically by simulating hundreds of synthetic storm surge scenarios to produce flood hazard maps for state and municipalities. Subgrid ADCIRC could drastically reduce these studies' computational and monetary cost.

These results do indicate paths for future work, specifically in the drawdown and underprediction of water levels at the LC2a gauge, and the consistent underprediction of water levels by the subgrid simulation along the main channel thalweg in the Calcasieu Lake test case (Figs. 7 and 8). In those tests, the coarse subgrid consistently under-predicted water levels when compared to the fine traditional. This may be attributed to an over-estimation of friction by the subgrid model, and increases in Manning's n values from interpolation to the coarsened mesh. Volp et al. (2013) presented a scheme to correct this over-prediction and take advantage of high resolution roughness data. Implementation of a friction correction should lend itself well to the current subgrid framework present in the code. The drawdown that occurred at this location as the storm made landfall is present in both the fine traditional and coarse subgrid simulations; the water levels are decreased to -1.0 m, or about 1.3 m below the gauge data. These differences can largely be attributed to the gauge installation. The LC2a gauge was a barotropic pressure sensor mounted sub-aerially at 0.303 m NAVD88. Therefore, the sensor was not able to measure a drawdown below 0.303 m. The flattening of the gauge data from 0000 UTC to 0500 UTC 24 September indicates that the water level dropped below the gauge mount elevation, thus there is no way of verifying prediction accuracy during this time period. Other factors that could have affected model accuracy include poor representation of vertical features like roadways and levees that lie along the lake's edge and act as hydraulic barriers to keep water in the lake during the storm. These hydraulic features can be better represented with cell clones, which prevent flow between non-hydraulically connected features. Previous implementations of cell clones have used numerical schemes in which the velocities are located along the cell edge, which allows for connectivity and/or blocking of flows within the cell (Begmohammadi et al., 2021; Casulli, 2019). This capability will be challenging to implement in ADCIRC, because the model defines the flow variables at the vertices of each element, and thus it is not straight-forward to identify connectivity for each clone. However, the capability would better represent the blocking of flow due to subgrid obstacles.

5. Conclusions

In this study, subgrid corrections were implemented in the widely-used ADCIRC model for storm surge and coastal flooding. These corrections were tested on a variety of domains and showed promising results both for idealized and realistic tides and storm surge. Subgrid ADCIRC is able to capture hydraulic connectivity and water level calculations on coarsened meshes in which small hydraulic features are not resolved at the mesh scale. This improvement is attributed to subgrid ADCIRC's ability to represent small hydraulic features contained within partially wet elements. Without the use of sufficiently small element sizes, traditional ADCIRC cannot resolve these features. The inclusion of partially wet elements to solve for water levels and velocities was achieved by redesigning the wetting and drying routine within the code to solely rely on the wet area fraction (ϕ) when determining the wet/dry state of an element or vertex.

The main contributions and findings of this study are:

 Extension of subgrid corrections using the widely used ADCIRC storm surge model with hurricane strength forcing. The addition of subgrid corrections to ADCIRC's governing equations allowed for use of partially wet elements and vertices. This permits modified storm forcing at the wet/dry boundary by way of the wet area fraction. Testing on the realistic Calcasieu Lake domain using forcing from Rita (2005) demonstrated that these modifications give good overall matches to gauge hydrographs when run on coarsened meshes.

- 2. Subgrid corrections in ADCIRC allow for increases in accuracy and hydraulic connectivity when running on significantly coarsened meshes. In a forecasting scenario, this would give emergency managers and decision makers a more-accurate prediction of when flood waters will arrive and recede. This will allow them to use the best information possible when deciding evacuation times and coordinating search and rescue missions.
- 3. For a given grid, introducing subgrid corrections to ADCIRC increases computational cost to the code; however, these costs are small when compared to the efficiency gained by running on coarsened meshes. In our current implementation, the coarse subgrid storm surge simulation on Calcasieu Lake is approximately 40% slower than its coarse traditional counterpart. Nevertheless, it ran 32 times faster than the fine simulation and produced comparable results, reducing the simulation run time from 42.2 h to 1.3 h.

With these additions, subgrid ADCIRC has the potential to predict coastal flooding at a fraction of the computational cost. Further investigation is needed as to whether this efficiency can be further increased with adjustments to the model time step. Future work will include tests of subgrid ADCIRC on ocean-scale domains, the use of ensemble frameworks to forecast storm surge, and the use of additional correction such as friction to further improve model results.

CRediT authorship contribution statement

Johnathan L. Woodruff: Conceptualization, Methodology, Software, Validation, Formal analysis, Investigation, Resources, Data curation, Writing – original draft, Writing – review & editing, Visualization. J.C. Dietrich: Conceptualization, Methodology, Software, Resources, Writing – original draft, Writing – review & editing, Supervision, Project administration, Funding acquisition. D. Wirasaet: Conceptualization, Methodology, Software, Writing – review & editing, Supervision. A.B. Kennedy: Conceptualization, Methodology, Writing – review & editing, Supervision, Project administration, Funding acquisition. D. Bolster: Conceptualization, Writing – review & editing, Supervision, Project administration, Funding acquisition. Z. Silver: Software. S.D. Medlin: Visualization. R.L. Kolar: Methodology.

Declaration of competing interest

The authors declare that they have no known competing financial interests or personal relationships that could have appeared to influence the work reported in this paper.

Acknowledgments

This study was supported by National Science Foundation, United States grants ICER 1664037 and 1664040. The support of the National Science Foundation and the US Army Corps of Engineers is greatly appreciated by all contributors to this project.

Appendix. Averaged governing equations for adcirc

The upscaled governing equations stated in Section 2.3 are derived by applying a formal averaging technique (Whitacker, 1999) to the standard 2D shallow water equations written in the conservative form. By following such a technique, we define a mesh-scale average of any flow quantity ${\cal Q}$ as:

$$\langle Q \rangle_G = \frac{1}{A_G} \iint_{A_W} Q \, \mathrm{d}A, \tag{A.1}$$

where A_G denotes the mesh area and A_W the wet area within A_G (note that A_G and A_W are related through Eq. (2)). In addition, an alternative average use in the wet average (commonly known as intrinsic phase average) defined by:

$$\langle Q \rangle_W = \frac{1}{A_W} \iint_{A_W} Q \, dA. \tag{A.2}$$

In addition, the following rules (Whitacker, 1985) are used to interchange differentiation with respect to time and space and time-dependent spatial integration. In the formula below, U_B denotes the velocity of the potentially moving boundary, $\mathbf{n}_s = (n_{s,x}, n_{s,y})$ is an outward-pointing unit vector normal to the wet/dry boundary, Γ_W is the wet/dry boundary, and the subscript r denotes a dummy notation for the x or y coordinates.

$$\left\langle \frac{\partial Q}{\partial t} \right\rangle_G = \frac{\partial \langle Q \rangle_G}{\partial t} - \frac{1}{A_G} \int_{\Gamma_W} Q U_B \cdot \mathbf{n}_s \, dS, \tag{A.3}$$

and

$$\left\langle \frac{\partial Q}{\partial r} \right\rangle_G = \frac{\partial \langle Q \rangle_G}{\partial r} + \frac{1}{A_G} \int_{\Gamma_W} \mathbf{n}_{s,r} Q \, \, \mathrm{d}S. \tag{A.4}$$

The development of subgrid equations involves roughly applying (A.2) to the mass and momentum equations, making use of (A.3) and (A.4), and determining closures for terms that are not uniquely defined by the coarsened mesh-scale variables. The following subsections describe the development of the averaged mass equation, the averaged momentum equations, and the reformulation of the averaged continuity equation into the GWCE form.

A.1. Averaged primitive continuity equation

The primitive continuity equation is:

$$\frac{\partial H}{\partial t} + \frac{\partial UH}{\partial x} + \frac{\partial VH}{\partial y} = 0, \tag{A.5}$$

in which $H=h+\zeta$ is the total water depth, h is the bathymetric depth measured positive downwards from a reference datum, ζ is the water surface elevation measured positive upwards from the datum, U and V are the depth-averaged horizontal velocity components in the x-and y-directions respectively. The mesh-scale averaging of each term is described below.

First, for the local rate of change in time, we use (A.3) to pull the time derivative out of the integral, more specifically,

$$\begin{split} \left\langle \frac{\partial H}{\partial t} \right\rangle_{G} &= \frac{1}{A_{G}} \iint_{A_{W}} \frac{\partial H}{\partial t} \, \mathrm{d}A \\ &= \frac{1}{A_{G}} \frac{\partial}{\partial t} \iint_{A_{W}} H \, \mathrm{d}A - \frac{1}{A_{G}} \int_{\Gamma_{W}} H \left(\boldsymbol{U}_{B} \cdot \boldsymbol{\mathbf{n}}_{s} \right) \, \mathrm{d}S. \end{split} \tag{A.6}$$

Because H=0 at the wet/dry front, we eliminate the boundary integral and obtain

$$\left\langle \frac{\partial H}{\partial t} \right\rangle_{G} = \frac{1}{A_{G}} \iint_{A_{W}} \frac{\partial H}{\partial t} \, dA = \frac{1}{A_{G}} \frac{\partial}{\partial t} \iint_{A_{W}} H \, dA = \frac{\partial \langle H \rangle_{G}}{\partial t}, \tag{A.77}$$

which is now temporal rate of change of the averaged total water depth. Next, for the volume flux in the x-direction, we apply the spatial averaging (A.4) to pull the spatial derivative out of the integral, more precisely.

$$\left\langle \frac{\partial UH}{\partial x} \right\rangle_{G} = \frac{1}{A_{G}} \iint_{A_{W}} \frac{\partial UH}{\partial x} dA$$

$$= \frac{1}{A_{G}} \frac{\partial}{\partial x} \iint_{A_{W}} UH dA + \frac{1}{A_{G}} \int_{I_{W}} UH \mathbf{n}_{s,x} dS. \tag{A.8}$$

Again H=0 at the wet/dry boundary, we eliminate the boundary integral and have:

$$\left\langle \frac{\partial UH}{\partial x} \right\rangle_G = \frac{1}{A_G} \iint_{A_W} \frac{\partial UH}{\partial x} \, \mathrm{d}A = \frac{1}{A_G} \frac{\partial}{\partial x} \iint_{A_W} UH \, \mathrm{d}A = \frac{\partial \langle UH \rangle_G}{\partial x}. \tag{A.9}$$

The interchange between differentiation and integration in the averaging of the last term, the volume flux in the y-direction, can be done in an analogous way. After above manipulation, the averaged primitive continuity equation becomes

$$\frac{\partial \langle H \rangle_G}{\partial t} + \frac{\partial \langle UH \rangle_G}{\partial x} + \frac{\partial \langle VH \rangle_G}{\partial y} = 0. \tag{A.10}$$

By postulating that ζ varies very slowly within A_W , one has $\langle H \rangle_G = \frac{1}{A_G} \int_{z=-i m}^{z=-i \zeta} \iint_{A_G} max(0,b+z) \, \mathrm{d}A \, \mathrm{d}z.$ As a consequence, we can rewrite Eq. (A.10) as

$$\phi \frac{\partial \langle \zeta \rangle_W}{\partial t} + \frac{\partial \langle UH \rangle_G}{\partial x} + \frac{\partial \langle VH \rangle_G}{\partial y} = 0, \tag{A.11}$$

which is the final averaged form of the primitive continuity equation to be considered in the reformulation into the GWCE described below in Appendix A.3.

Note that in this study, we consider $\langle UH \rangle_G$ as the variable to be solved for. Instead of using (A.2), the velocity when required is computed from the following formula

$$\langle U \rangle = \frac{\iint_{A_W} H U \, dA}{\iint_{A_W} H \, dA} = \frac{\langle H U \rangle_G}{\langle H \rangle_G},$$
 (A.12)

or equivalently

$$\langle U \rangle \langle H \rangle_G = \langle U H \rangle_G. \tag{A.13}$$

It is worth mentioning that the so-called volume-averaged velocity defined above has an advantage over an averaged velocity defined by (A.2) in that it permits a substitution of $\langle UH \rangle_G$ by $\langle U \rangle \langle H \rangle_G$ in the governing equation without the need to resort to a more complicated closure. From this point forward, unless otherwise indicated, the notation $\langle U \rangle$ is understood as the volume averaged velocity. Note that various forms of governing equations presented (Kennedy et al., 2019) are obtained from making use of (A.13); they are intended for the solution where $\langle U \rangle$ is chosen as an unknown variable.

A.2. Averaged conservative momentum equations

We now average to the mesh scale the conservative momentum equations, including terms for the barotropic pressure gradient and lateral momentum-mixing stress terms. Consider the momentum equation in the x-direction:

$$\frac{\partial UH}{\partial t} + \frac{\partial UUH}{\partial x} + \frac{\partial UVH}{\partial y} - fVH = -gH\frac{\partial \left[\zeta + P_A\right]}{\partial x} + \frac{\tau_{sx}}{\rho_0} - \frac{\tau_{bx}}{\rho_0} + M_x.$$
(A.14)

It can be verified through the use of (A.3) and (A.4) and H=0 at the wet/dry boundary that the mesh scale averaging of (A.14) is equivalent to:

$$\begin{split} &\frac{\partial \langle UH \rangle_G}{\partial t} + \frac{\partial \langle UUH \rangle_G}{\partial x} + \frac{\partial \langle VUH \rangle_G}{\partial y} - f \langle VH \rangle_G = - \left\langle gH \frac{\partial \zeta}{\partial x} \right\rangle_G \\ &- g \langle H \rangle_G \frac{\partial P_A}{\partial x} + \left\langle \frac{\tau_{sx}}{\rho_0} \right\rangle_G - \left\langle \frac{\tau_{bx}}{\rho_0} \right\rangle_G + \langle M_x \rangle. \end{split} \tag{A.15}$$

In the above equation, the Coriolis parameter f and the atmospheric pressure P_A are assumed to vary at a spatial scale much larger than the grid scale and hence can be moved out of their respective integral terms. There is no unique way to define the averaging of convective momentum, bottom friction, surface gradients, and lateral mixing stresses in terms of the mesh-scale quantities $\langle H \rangle_G, \langle UH \rangle_G, \langle U \rangle$; further assumptions to be described below are therefore required to close the system.

For the convective accelerations, we chose the closure of the form written below:

$$\langle UUH\rangle_G = C_{UU}\langle U\rangle\langle UH\rangle_G, \langle UVH\rangle_G = C_{UV}\langle U\rangle\langle VH\rangle_G,$$

which resemble the particular forms of the convective momentum considered in ADCIRC (see Equation (2.2) on p.15 of the ADCIRC theory report (Luettich and Westerink, 2004)) with additional correction coefficients C_{UU} and C_{UV} .

For the surface gradient pressure term, we consider the following closure:

$$\begin{split} g\left\langle H\frac{\partial P_{A}}{\partial x}\right\rangle _{G} &= g\langle H\rangle _{G}\frac{\partial P_{A}}{\partial x} = g\phi\left\langle H\frac{\partial \zeta}{\partial x}\right\rangle _{W}\\ &= gC_{\zeta}\phi\langle H\rangle _{W}\frac{\partial \langle \zeta\rangle _{W}}{\partial x} = gC_{\zeta}\langle H\rangle _{G}\frac{\partial \langle \zeta\rangle _{W}}{\partial x}, \end{split} \tag{A.16}$$

where C_{ζ} is an additional correction coefficient. Although counterintuitive, numerical evidences demonstrate in Kennedy et al. (2019) indicated that C_{ζ} is clearly needed in some cases.

For the surface stress term, we consider the quadratic drag law for the surface stress caused by wind:

$$\left\langle \frac{\tau_{sx}}{\rho_0} \right\rangle_G = \phi \left\langle \frac{\tau_{sx}}{\rho_0} \right\rangle_W = \phi \frac{\rho_a}{\rho_0} C_D \left| \boldsymbol{W}_{10} \right| W_{10,x}, \tag{A.17}$$

where ρ_a denotes the air density and $\boldsymbol{W}_{10} = (W_{10,x}, W_{10,x})$ denotes the 10 m wind velocity assumed to be known (wind data comes typically from a numerical model with a spatial scale greater than the grid scale considered in the surge model).

The bottom stress τ_{bx} is assumed to obey a quadratic bottom friction law and the closure below is considered:

$$\left\langle \frac{\tau_{bx}}{\rho_0} \right\rangle_G = \phi \left\langle \frac{\tau_{bx}}{\rho_0} \right\rangle_W = \phi \left\langle \frac{C_f |\mathbf{U}| UH}{H} \right\rangle_W = \phi C_{M,f} \frac{|\mathbf{U}| \langle UH \rangle_W}{\langle H \rangle_W}, \tag{A.18}$$

where $C_{M,f}$ is to-be-determined equivalent frictional coefficients that may depend on water surface elevations. In this work, for simplicity, $C_{M,f}$ is taken to be:

$$C_{M,f} = \frac{g\langle n \rangle_W^2}{\langle H \rangle_W^{1/3}},\tag{A.19}$$

where $\langle n \rangle_W$ is a value characterizing the Manning's roughness coefficient of the wet area.

Finally, consider the average of the lateral mixing term:

$$\langle M_{x} \rangle_{G} = \left\langle \frac{\partial H \tau_{xx}}{\partial x} + \frac{\partial H \tau_{yx}}{\partial y} \right\rangle_{G}$$

$$= \frac{1}{A_{G}} \frac{\partial}{\partial x} \iint_{A_{W}} H \tau_{xx} \, dA + \frac{1}{A_{G}} \int_{\Gamma_{W}} H \tau_{xx} \mathbf{n}_{s,x} \, dS$$

$$+ \frac{1}{A_{G}} \frac{\partial}{\partial y} \iint_{A_{W}} H \tau_{yx} \, dA + \frac{1}{A_{G}} \int_{\Gamma_{W}} H \tau_{yx} \mathbf{n}_{s,y} \, dS$$

$$= \frac{\partial \langle H \tau_{xx} \rangle_{G}}{\partial x} + \frac{\partial \langle H \tau_{yx} \rangle_{G}}{\partial y}.$$
(A.20)

Boundary integrals go to zero because H=0 at the wet/dry boundary. Indeed, the vertically-integrated lateral terms $H\tau_{xx}$ and $H\tau_{yx}$ by itself require a closure assumption. ADCIRC supports several lateral closures. Here, we consider one specific form of such closures, more precisely:

$$H\tau_{xx}=\widetilde{E}_h\frac{\partial UH}{\partial x}, H\tau_{yx}=\widetilde{E}_h\frac{\partial UH}{\partial y}.$$

The grid-average of these lateral closures are approximated as:

$$\langle H\tau_{xx}\rangle_G = \widetilde{E}_h \frac{\partial \langle UH\rangle_G}{\partial x}, \langle H\tau_{yx}\rangle_G = \widetilde{E}_h \frac{\partial \langle UH\rangle_G}{\partial y},$$
 (A.21)

where \tilde{E}_h is a grid scale eddy viscosity (potentially of different value than that used in the high-resolution calculation).

With the closure terms given above, the averaged momentum equation in the x-direction becomes:

$$\begin{split} &\frac{\partial \langle UH \rangle_G}{\partial t} + g C_\zeta \langle H \rangle_G \frac{\partial \langle \zeta \rangle_W}{\partial x} = -\frac{\partial C_{UU} \langle U \rangle \langle UH \rangle_G}{\partial x} - \frac{\partial C_{VU} \langle V \rangle \langle UH \rangle_G}{\partial y} \\ &+ f \langle VH \rangle_G - g \langle H \rangle_G \frac{\partial P_A}{\partial x} + \phi \left\langle \frac{\tau_{sx}}{\rho_0} \right\rangle_W - \frac{g \langle n \rangle_W^2 |\langle U \rangle |\langle UH \rangle_G}{\langle H \rangle_W^{4/3}} \\ &+ \frac{\partial}{\partial x} \widetilde{E}_h \frac{\partial \langle UH \rangle_G}{\partial x} + \frac{\partial}{\partial y} \widetilde{E}_h \frac{\partial \langle UH \rangle_G}{\partial y}. \end{split}$$

Similarly, the averaged momentum equation in the *y*-direction with closure terms is:

$$\begin{split} &\frac{\partial \langle VH \rangle_{G}}{\partial t} + gC_{\zeta} \langle H \rangle_{G} \frac{\partial \langle \zeta \rangle_{W}}{\partial y} = -\frac{\partial C_{UV} \langle U \rangle \langle VH \rangle_{G}}{\partial x} - \frac{\partial C_{VV} \langle V \rangle \langle VH \rangle_{G}}{\partial y} \\ &- f \langle UH \rangle_{G} - g \langle H \rangle_{G} \frac{\partial P_{A}}{\partial y} + \phi \left\langle \frac{\tau_{sy}}{\rho_{0}} \right\rangle_{W} - \frac{g \langle n \rangle_{W}^{2} |\langle U \rangle |\langle VH \rangle_{G}}{\langle H \rangle_{W}^{4/3}} \\ &+ \frac{\partial}{\partial x} E_{h} \frac{\partial \langle VH \rangle_{G}}{\partial x} + \frac{\partial}{\partial y} E_{h} \frac{\partial \langle VH \rangle_{G}}{\partial y}. \end{split}$$

$$(A.23)$$

The final step is to select the correction coefficients. In this work, we consider a so-called 'Level 0' closure (Kennedy et al., 2019), in which: $C_{UU} = C_{UV} = C_{VU} = C_{VV} = 1$, $C_{\zeta} = 1$. Then the only non-unity closure is the wet-area fraction, as shown in the final Eqs. (5) and (6).

A.3. Averaged generalized wave continuity equation

Then the GWCE is formed by differentiating Eq. (A.11) with respect to time, adding to this (A.11) multiplied by a positive spatially-varying numerical parameter τ_0 . This leads to:

$$\frac{\partial}{\partial t} \left(\phi \frac{\partial \langle \zeta \rangle_W}{\partial t} \right) + \tau_0 \phi \frac{\partial \langle \zeta \rangle_W}{\partial t} + \frac{\partial \langle \tilde{J}_x \rangle_G}{\partial x} + \frac{\partial \langle \tilde{J}_y \rangle_G}{\partial y} - \langle UH \rangle_G \frac{\partial \tau_0}{\partial x} - \langle VH \rangle_G \frac{\partial \tau_0}{\partial y} = 0,$$
(A.24)

where

$$\langle \tilde{J}_x \rangle_G = \frac{\partial \langle UH \rangle_G}{\partial t} + \tau_0 \langle UH \rangle_G, \tag{A.25}$$

and

$$\langle \tilde{J}_{y} \rangle_{G} = \frac{\partial \langle VH \rangle_{G}}{\partial t} + \tau_{0} \langle VH \rangle_{G}. \tag{A.26}$$

The time derivative terms $\frac{\partial \langle UH \rangle_G}{\partial t}$ and $\frac{\partial \langle VH \rangle_G}{\partial t}$ in the above equation are further eliminated by means of the momentum equation (A.22) and (A.23). With the Level 0 closure we obtain the final form of the GWCE as it appears in Eq. (7) repeated below:

$$\begin{split} \phi \frac{\partial^2 \langle \zeta \rangle_W}{\partial t^2} &+ \frac{\partial \phi}{\partial t} \frac{\partial \langle \zeta \rangle_W}{\partial t} + \tau_0 \phi \frac{\partial \langle \zeta \rangle_W}{\partial t} \\ &- \frac{\partial}{\partial x} \left(g \langle H \rangle_G \frac{\partial \langle \zeta \rangle_W}{\partial x} \right) - \frac{\partial}{\partial y} \left(g \langle H \rangle_G \frac{\partial \langle \zeta \rangle_W}{\partial y} \right) \\ &+ \frac{\partial \langle \tilde{J}_x \rangle_G}{\partial x} + \frac{\partial \langle \tilde{J}_y \rangle_G}{\partial y} - \langle U H \rangle_G \frac{\partial \tau_0}{\partial x} - \langle V H \rangle_G \frac{\partial \tau_0}{\partial y} = 0, \end{split}$$

where:

$$\langle \tilde{J}_x \rangle_G = (\text{RHS of (A.22)}) + \tau_0 \langle UH \rangle_G,$$

and:

$$\langle \tilde{J}_{\nu} \rangle_G = (\text{RHS of (A.23)}) + \tau_0 \langle VH \rangle_G.$$

Note that for $\langle H \rangle_G > 0$ (i.e. in fully wet or partial wet areas) the GWCE is a second order wave equation.

A.4. Finite element discretization

In this study, the ADCIRC solvers were kept largely the same, the GWCE is solved implicitly via the use of a global mass matrix, while the momentum equations are solved semi-implicitly. Both elementand vertex-based quantities are used in these solutions. On each time marching step, the GWCE (Eq. (7)) uses elementally-averaged quantities (Fig. 1) to find a vertex-averaged water surface elevation $\langle \zeta \rangle_W$. This quantity is then used to look up the corresponding vertex-averaged total water depth $\langle H \rangle_W$, wet area fraction ϕ , and wet averaged Manning's $n \langle n \rangle_W$, which are used along with elementally-averaged quantities to solve Eqs. (5) and (6) for the vertex-averaged water velocities. Because we are solving averaged equations, the solutions for $\langle \zeta \rangle_W$, $\langle U \rangle$, and

(A.22)

 $\langle V \rangle$ are appropriately averaged. Therefore, no further manipulation is required.

The only change was the addition of the $\frac{\partial \phi}{\partial t} \frac{\partial \langle \zeta \rangle_W}{\partial t}$ which was discretized in the following way:

$$\frac{\partial \phi}{\partial t} \frac{\partial \langle \zeta \rangle_W}{\partial t} = \sum_{n=1}^{NE_j} \frac{A_n}{12} \frac{\partial \overline{\phi}_n}{\partial t} \sum_{i=1}^3 \boldsymbol{\Phi}_{i,j} \frac{\partial \langle \zeta \rangle_{W_i}}{\partial t},$$

whore

$$\frac{\partial \overline{\phi}_n}{\partial t} = \frac{\overline{\phi}_n^s - \overline{\phi}_n^{s-1}}{\Delta t} \quad \text{and} \quad \frac{\partial \langle \zeta \rangle_{W_i}}{\partial t} = \frac{\langle \zeta \rangle_i^{s+1} - \langle \zeta \rangle_i^{s-1}}{2\Delta t}.$$

Here, A_n is the area of element n, NE_j is the number of elements containing node j, $\overline{\phi}_n$ is the average wet area fraction over element n, $\Phi_{i,j}$ is the weighting function, and s is the current timestep.

References

- Bates, P.D., Hervouet, J.M., 1999. A new method for moving-boundary hydrodynamic problems in shallow water. Proc. R. Soc. Lond. Ser. A Math. Phys. Eng. Sci. 455, 3107–3128.
- Begmohammadi, A., Wirasaet, D., Silver, Z., Bolster, D., Kennedy, A.B., Dietrich, J.C., 2021. Subgrid surface connectivity for storm surge modelling. Adv. Water Resour. 153.
- Berenbrock, C., Mason, R., Blanchard, S., 2008. Mapping hurricane Rita inland storm tide. In: 4th International Symposium on Flood Defence.
- Bilskie, M.V., Coggin, D., Hagen, S.C., Medeiros, S.C., 2015. Terrain-driven unstructured mesh development through semi-automatic vertical feature extraction. Adv. Water Resour. 86, 102–118.
- Blanton, B.O., McGee, J., Fleming, J.G., Kaiser, C., Kaiser, H., Lander, H., Luettich, R.A., Dresback, K.M., Kolar, R.L., 2012. Urgent Computing of Storm Surge for North Carolina's Coast. In: Proceedings of the International Conference on Computational Science. vol. 9, pp. 1677–1686.
- Burrough, P.A., McDonnell, R.A., 1998. Principles of Geographical Information Systems. Oxford, New York: Oxford University Press.
- Casulli, V., 2009. A high-resolution wetting and drying algorithm for free-surface hydrodynamics. Numer. Methods Fluids 60, 391–408.
- Casulli, V., 2019. Computational grid, subgrid, and pixels. Internat. J. Numer. Methods Fluids 90, 140–155.
- Cheung, K.F., Phadke, A.C., Wei, Y., Rojas, R., Douyere, Y.J.M., Martino, C.D., Houston, S.H., Liu, P.L.F., Lynett, P.J., Dodd, N., Liao, S., Nakazaki, E., 2003. Modeling of storm-induced coastal flooding for emergency management. Ocean Eng. 30, 1353–1386.
- Cialone, M.A., Grzegorzewski, A.S., Mark, D.J., Bryant, M.A., Massey, T.C., 2017.
 Coastal-storm model development and water-level validation for the North Atlantic
 Coast comprehensive study. J. Waterw. Port Coast. Ocean Eng. 143.
- CoreLogic, 2020. 2020 storm surge report. https://www.corelogic.com/downloadable-docs/storm-surge-report-20200528-screen-2.pdf [Retrieved 20 October 2020].
- Deb, M., Ferreira, C.M., 2016. Simulation of cyclone-induced storm surges in the low-lying delta of Bangladesh using coupled hydrodynamic and wave model (SWAN + ADCIRC). J. Flood Risk Manag. 11, S750–S765.
- Defina, A., 2000. Two-dimensional shallow flow equations for partially dry areas. Water Resour. Res. 36, 3251–3264.
- Dick, C.G., Tromble, E.M., Dresback, K.M., Kolar, R.L., 2013. Implementation and analysis of a partial-element wetting and drying framework for generalized wave continuity equation-based hydrodynamic models. 72, pp. 1015–1033.
- Dietrich, J.C., Bunya, S., Westerink, J.J., Ebersole, B.A., Smith, J.M., Atkinson, J.H., Jensen, R.E., Resio, D.T., Luettich, R.A., Dawson, C.N., Cardone, V.J., Cox, A.T., Powell, M.D., Westerink, H.J., Roberts, H.J., 2010. A high-resolution coupled riverine flow, tide, wind, wind wave and storm surge model for Southern Louisiana and Mississippi: Part II synoptic description and analysis of Hurricanes Katrina and Rita. Mon. Weather Rev. 138, 378–404.
- Dietrich, J.C., Tanaka, S., Westerink, J.J., Dawson, C.N., Luettich, R.A., Zijlema, M., Holthuijsen, L.H., Smith, J.M., Westerink, L.G., Westerink, H.J., 2012. Performance of the unstructured-mesh, SWAN+ADCIRC model in computing hurricane waves and surge. J. Sci. Comput. 52, 468–497.
- Dietrich, J.C., Zijlema, M., Westerink, J.J., Holthuijsen, L.H., Dawson, C.N., Luettich, R.A., Jensen, R.E., Smith, J.M., Stelling, G.S., Stone, G.W., 2011. Modeling hurricane waves and storm surge using integrally-coupled, scalable computations. Coast. Eng. 58, 45–65.
- Dresback, K.M., Fleming, J.G., Blanton, B.O., Kaiser, C., Gourley, J.J., Tromble, E.M., Luettich, R.A., Kolar, R.L., Hong, Y., Van Cooten, S., Vergara, H.J., Flamig, Z., Lander, H.M., Kelleher, K.E., Nemunaitis-Monroe, K.L., 2013. Skill assessment of a real-time forecast system utilizing a coupled hydrologic and coastal hydrodynamic model during hurricane irene (2011). Cont. Shelf Res. 71, 78–94.
- Emanuel, K., 2020. Evidence that hurricanes are getting stronger. Proc. Natl. Acad. Sci. USA 117, 13194–13195.
- U.S. Army Corps of Engineers, 2015. North Atlantic Coast Comprehensive Study: Resilient Adaption to Increasing Risk. Technical Report, U.S. Army Corps of Engineers.

- Federal Emergency Management Agency, 2019. Guidance for flood risk analysis and mapping: Determination of wave characteristics. Technical report.
- Fleming, J., Fulcher, C., Luettich, R.A., Estrade, B., Allen, G., Winer, H., 2008. A real time storm surge forecasting system using ADCIRC. In: Estuarine and Coastal Modeling (2007). pp. 893–912.
- Gao, J., 2018. On the Surface Wind Stress for Storm Surge Modeling. University of North Carolina at Chapel Hill. http://dx.doi.org/10.17615/zpeb-7k73.
- Garratt, J.R., 1977. Review of drag coefficients over oceans and continents. Mon. Weather Rev. 105, 915–929.
- Helderop, Edward, Grubesic, Tony H., 2019. Hurricane storm surge in Volusia County, Florida: evidence of a tipping point for infrastructure damage. Disasters 43, 157, 180
- Hope, M.E., Westerink, J.J., Kennedy, A.B., Kerr, P.C., Dietrich, J.C., Dawson, C.N., Bender, C.J., Smith, J.M., Jensen, R.E., Zijlema, M., Holthuijsen, L.H., Luettich Jr, R.A., Powell, M.D., Cardone, V.J., Cox, A.T., Pourtaheri, H., Roberts, H.J., Atkinson, J.H., Tanaka, S., Westerink, H.J., Westerink, L.G., 2013. Hindcast and validation of hurricane ike (2008) waves, forerunner, and storm surge. J. Geophys. Res. Oceans 118. 4424–4460.
- Kennedy, A.B., Wirasaet, D., Begmohammadi, A., Sherman, T., Bolster, D., Dietich, J.C., 2019. Subgrid theory for storm surge modeling. Ocean Model. 144.
- King, I., 2001. Modeling of marshes and wetlands. J. Coast. Res. 27, 76-87.
- Kinnmark, I., 1986. The shallow water wave equations: Formulation, analysis and application. In: Brebbia, C.A., Orszag, S.A. (Eds.), Lecture Notes in Engineering. vol. 15, Springer-Verlag, pp. 12–26.
- Knabb, R.D., Brown, D.P., Rhome, J.R., 2005. Tropical Cyclone Report, Hurricane Rita, 18–26 September 2005. Technical Report, National Hurricane Center.
- Lin, N., Chavas, D., 2012. On hurricane parametric wind and applications in storm surge modeling. J. Geophys. Res. 117.
- Luettich, R.A., Westerink, J.J., 1995. Implementation and testing of elemental flooding and drying in the ADCIRC hydrodynamic model. Technical Report, U.S. Army Corps of Engineers, Vicksburg MS.
- Luettich, R.A., Westerink, J.J., 2004. Formulation and numerical implementation of the 2D/3D ADCIRC finite element model version 44.XX. University of North Carolina at Chapel Hill, https://adcirc.org/files/2018/11/adcirc_theory_2004_12_08.pdf.
- Luettich, R.A., Westerink, J.J., Scheffner, N.W., 1992. ADCIRC: An Advanced Three-Dimensional circulation model for shelves coasts and estuaries, report 1: Theory and methodology of ADCIRC-2DDI and ADCIRC-3DL. Technical Report, United States Army Corps of Engineers.
- Medeiros, S.C., Hagen, S.C., 2013. Review of wetting and drying algorithms for numerical tidal flow models. Internat. J. Numer. Methods Fluids 71, 473–487.
- National Hurricane Center, 2020. Sea, lake, and overland surges from Hurricanes (SLOSH). [Retrieved 22 December 2020], https://www.nhc.noaa.gov/surge/slosh.php.
- National Oceanic and Atmospheric Administration, 2020. Data access viewer. https://coast.noaa.gov/dataviewer/#/lidar/search/ [Retrieved 20 October 2020].
- National Oceanic and Atmospheric Administration, 2021. Data access viewer. [Retrieved 26 January 2021], https://coast.noaa.gov/dataviewer/#/landcover/search/.
- Roberts, K.J., Pringle, W.J., Westerink, J.J., 2019. OceanMesh2D 1.0: MATLAB-based software for two-dimensional unstructured mesh generation in coastal ocean modeling. Geoscientific Model Development 12, 1847–1868. http://dx.doi.org/10.5194/gmd-12-1847-2019.
- Roig, L.C., 1994. Hydrodynamic Modeling of Flows in Tidal Wetlands. University of California Davis.
- Rucker, C.A., Tull, N., Dietrich, J.C., Langan, T.E., Mitasova, H., Flemming, J.G., Blanton, B.O., Luettich, R.A., 2021. Downscaling of real-Time Coastal flooding predictions for decision support. Nat. Hazards 107, 1341–1369. http://dx.doi.org/ 10.1007/s11069-021-04634-8.
- Sehili, A., Lang, G., Lippert, C., 2014. High-resolution subgrid models: background, grid generation, and implementation. Ocean Dyn. 64, 519–535.
- Tanaka, S., Bunya, S., Westerink, J.J., Dawson, C.N., Luettich, R.A., 2011. Scalability of an unstructured grid continuous Galerkin based Hurricane storm surge model. J. Sci. Comput. 46, 329–358.
- U.S. Geological Survey, 2020a. Coastal national elevation database (coNED) applications project. https://topotools.cr.usgs.gov/topobathy_viewer/ [Retrieved 20 October 2020].
- U.S. Geological Survey, 2020b. Flood event viewer. https://stn.wim.usgs.gov/FEV/ #Rita [Retrieved 29 December 2020].
- Viero, D.P., 2019. Modelling urban floods using a finite element staggered scheme with an anisotropic dual porosity model. J. Hydrol. 568, 247–259.
- Volp, N.D., van Prooijen, B.C., Stelling, G.S., 2013. A finite volume approach for shallow water flow accounting for high-resolution bathymetry and roughness data. Water Resour. Res. 49, 4126–4135.
- Westerink, J.J., Luettich Jr, R.A., Feyen, J.C., Atkinson, J.H., Dawson, C.N., Roberts, H.J., Powell, M.D., Dunion, J.P., Kubatko, E.J., Pourtaheri, H., 2008. A basin to channel scale unstructured grid Hurricane storm surge model applied to Southern Louisiana. Mon. Weather Rev. 136, 833–864.
- Whitacker, S., 1985. A simple geometrical derivation of the spatial averaging theorem. Chemical Engineering Education 19.
- Whitacker, S., 1999. The Method of Volume Averaging. Kluwer Academic Publishers.
 Wu, G., Shi, F., Kirby, J.T., Mieras, R., Liang, B., Li, H., Shi, J., 2016. A pre-storage, subgrid model for simulating flooding and draining processes in salt marshes. Coast.

14